

1 **Climate variability and change of Mediterranean-type**  
2 **climates**

3 RICHARD SEAGER\*,

4 *Lamont Doherty Earth Observatory of Columbia University, Palisades, New York*

5 TIMOTHY J. OSBORN

6 *Climatic Research Unit, University of East Anglia, Norwich, United Kingdom*

YOCHANAN KUSHNIR

*Lamont Doherty Earth Observatory of Columbia University, Palisades, New York*

7 ISLA R. SIMPSON ,

*Climate and Global Dynamics Laboratory, National Center for Atmospheric Research, Boulder, Colorado*

8 JENNIFER NAKAMURA AND HAIBO LIU ,

*Lamont Doherty Earth Observatory of Columbia University, Palisades, New York*

---

\* *Corresponding author address:* Richard Seager, Lamont Doherty Earth Observatory of Columbia University, 61 Route 9W., Palisades, NY 10964. Email: seager@ldeo.columbia.edu

Submitted to *J. Climate* July 2018, revised November 2018, January 2019, LDEO Contribution Number XXXX.

## ABSTRACT

10 Mediterranean-type climates are defined by temperate, wet winters and hot or warm dry  
11 summers and exist at the western edges of five continents in locations determined by the  
12 geography of winter storm tracks and summer subtropical anticyclones. The climatology,  
13 variability and long term changes in winter precipitation in Mediterranean-type climates,  
14 and the mechanisms for model-projected near-term future change, are analyzed. Despite  
15 commonalities in terms of location in the context of planetary scale dynamics, the causes of  
16 variability are distinct across the regions. Internal atmospheric variability is the dominant  
17 source of winter precipitation variability in all Mediterranean-type climate regions, but only  
18 in the Mediterranean is this clearly related to annular mode variability. Ocean forcing of  
19 variability is a notable influence only for California and Chile. As a consequence, potential  
20 predictability of winter precipitation variability in the regions is low. In all regions, the  
21 trend in winter precipitation since 1901 is similar to that which arises as a response to  
22 changes in external forcing in the models participating in the Coupled Model Intercomparison  
23 Project Five. All Mediterranean-type climate regions, except in North America, have dried  
24 and the models project further drying over coming decades. In the northern hemisphere,  
25 dynamical processes are responsible: development of a winter ridge over the Mediterranean  
26 that suppresses precipitation and of a trough west of the North American west coast that  
27 shifts the Pacific stormtrack equatorward. In the southern hemisphere, mixed dynamic-  
28 thermodynamic changes are important that place a minimum in vertically integrated water  
29 vapor change at the coast and enhance zonal dry advection into Mediterranean-type climate  
30 regions inland.

# 31 1. Introduction

32 Mediterranean-type climates are defined by temperate, wet winters and warm or hot dry  
33 summers. The definition originates in the Mediterranean region itself. Here winter storms  
34 bring precipitation but the subtropical location ensures cold temperatures rarely occur and  
35 the precipitation is generally rain except at high elevations. The summers are dry, apart from  
36 localized regions of convection over land, and the subtropical location and clear skies under  
37 descending air allow for high temperatures. The dynamical origins of the Mediterranean  
38 climate are, in winter, its location at the poleward edge of the winter Hadley Cell and  
39 equatorward flank of the North Atlantic storm track and, in summer, its location under  
40 a vast area of subsidence extending from the North Atlantic subtropical high, across the  
41 Mediterranean and into east Asia and encompassing North Africa as well.

42 Because of the location of the Mediterranean climate and its generation in terms of  
43 planetary scale dynamics, it is not surprising that there are four other regions of the world  
44 with Mediterranean-type climates. These are the west coast of North America from north-  
45 ern Mexico to Washington State, central Chile, the far southwest tip of southern Africa  
46 and southwest Australia. All these regions have the same winter-dominated precipitation  
47 regime, temperate winter climates and hot or warm, dry summers. The climatological sim-  
48 ilarity of the world's Mediterranean-type climate regions (MCRs) translates into similar  
49 natural vegetation with sparse woodlands, grasses and shrubs that have been converted into  
50 similar agricultural uses for growing vines (primarily for wine), fruits, olives, wheat and  
51 nuts (di Castri and Mooney 1973), the bases of the so-called Mediterranean diet with its  
52 associated health benefits (Baich-Faig et al. 2011).

53 All of the MCRs lie in the subtropics to mid-latitudes and on the western edge of con-  
54 tinents. This location ensures a mild, maritime climate in winter with precipitation from  
55 storms in the extratropical storm tracks and, in the summer, warm to hot, dry summers  
56 under the influence of the eastern flanks of subtropical highs (Rodwell and Hoskins 2001;  
57 Seager et al. 2003b). The Mediterranean region itself is actually unique in that winter precip-  
58 itation occurs primarily within the Mediterranean storm track (Trigo et al. 1999; Campins  
59 et al. 2011; Lionello et al. 2006; Flocas et al. 2010), which is distinct from the North Atlantic

60 storm track, and the summer subsidence is east of the North Atlantic subtropical high and  
61 more related to a forced response to Asian monsoon heating (Rodwell and Hoskins 1996,  
62 2001; Simpson et al. 2015). Only the climates of Portugal and Morocco are strictly analogous  
63 in climate dynamical context to the four other Mediterranean-type climates.

64 All MCRs are overall semi-arid as a result of the highly seasonal precipitation and long  
65 dry summers and all struggle with water resources at the best of times. Lying between the  
66 more arid subtropics and the more humid extratropics they are locations of impactful climate  
67 variability and are highly vulnerable to intense and protracted droughts (e.g. Hurrell (1995);  
68 Smith et al. (2000); Risbey et al. (2009); Seager et al. (2014a); Cook et al. (2016); Garreaud  
69 et al. (2018)). Fire is a hazard common to Mediterranean-type climates too (Bowman et al.  
70 2017). In recent years California has experienced withering droughts (Seager et al. 2014a;  
71 Williams et al. 2015) and fires, Chile has also experienced drought and fire (Garreaud et al.  
72 2018), southwest Africa (around Cape Town) is enduring a severe drought (Wolski 2018;  
73 Simpkins 2018) and the Mediterranean and southwest Australia have experienced persistent  
74 dry conditions in recent decades (Allan and Haylock 1993; Kelley et al. 2011; Hoerling et al.  
75 2012; Delworth and Zeng 2014). In addition, climate change caused by rising greenhouse  
76 gases is expected to reduce precipitation in all MCRs other than California (Polade et al.  
77 2017) and warming will increase drought risk (Cook et al. 2014).

78 Given their same similar climates arising from comparable geographical locations with  
79 reference to continental geography and planetary scale circulation, it might be expected  
80 that the causes and character of climate variability and change would also be similar across  
81 the MCRs. There is an extensive literature addressing climate variability and change for  
82 the Mediterranean, California and, to some extent, Chile and somewhat less for southwest  
83 Africa and southwest Australia. However, while Polade et al. (2017) address climate change  
84 across the MCRs, to our knowledge there has yet to be a study that compares and contrasts  
85 both variability and change across the Mediterranean-type climates and places this within a  
86 mechanistic climate dynamics framework to achieve basic understanding. In this regard the  
87 similarities and differences will be informative as to the underlying processes influencing these  
88 climate regions. While all MCRs face similar climate problems, are the climate processes  
89 generating the variability and change the same or different?

90 In this paper we will address the following issues.

- 91 i. How similar are the climatology and variability of precipitation and temperature across  
92 the MCRs?
- 93 ii. What atmospheric circulation phenomena drive interannual variability of winter pre-  
94 cipitation of the MCRs? What is the relative role of ocean (sea surface temperature,  
95 SST) forcing compared to internal atmospheric variability?
- 96 iii. What are the trends in winter precipitation over the past century in the MCRs? Are  
97 they consistent with expectations, based on climate models, of change due to human-  
98 induced climate change?
- 99 iv. What are the dynamical and thermodynamical mechanisms that models project will  
100 cause declines in winter precipitation in all MCRs other than California?
- 101 v. What are the common processes that lead to similar variability and change across  
102 MCRs and what are the zonally and hemispherically asymmetric processes that lead  
103 to differences across MCRs?

104 We begin by describing the data and then present a series of observational analyses and  
105 simulations with SST-forced models to examine variability. We will then examine simulations  
106 from the Coupled Model Intercomparison Project Five (CMIP5) to diagnose projections of  
107 radiatively-forced change and determine the mechanisms responsible. A discussion of the  
108 commonalities and differences between MCRs from a climate dynamics perspective will follow  
109 and then we will offer conclusions.

## 110 **2. Mediterranean-type climate definition and observa-** 111 **tional data and model simulations used**

### 112 *a. Mediterranean-type climate type definition*

113 Our definition of MCRs follows the Köppen climate classification which divides climates  
114 with 1), winters that are temperate and the season of maximum precipitation and 2), dry

115 summers, into two types: *Csa* hot summers and *Csb* warm summers. The categorization is  
116 that of Leemans and Cramer (1991) and is provided with details at [http://iridl.ldeo.columbia.edu/SOURCES/.UN/.FAO/.NRMED/.SD/.Climate/.dataset\\_documentation.html#](http://iridl.ldeo.columbia.edu/SOURCES/.UN/.FAO/.NRMED/.SD/.Climate/.dataset_documentation.html#anchor2)  
117 [anchor2](#). The MCRs are shown on Figure 1. The Mediterranean, California and southwest  
118 Australia are dominated by the *Csa* hot summer type, and Chile and southwest southern  
119 Africa by the *Csb* warm type. Note that, according to the Koppen climate classification, the  
120 Pacific Northwest of North America is an MCR. Since, for example, Seattle is not commonly  
121 considered to have an MCR (but does have a climate similar to central Chile) we have broken  
122 the west coast of North America into the Pacific Northwest and the more commonly con-  
123 sidered MCR of California. We also ignore the warm summer MCR in southeast Australia  
124 because of its somewhat different location in the context of planetary scale circulations. We  
125 recognize that we are adopting a broad brush climatology-inspired definition of MCR. For a  
126 more nuanced and detailed description of MCRs see Aschmann (1973). To create climate  
127 quantities within the MCRs we use shapefiles available from the International Research In-  
128 stitute for Climate and Society corresponding to the *Csa* and *Csb* locations in Figure 1. The  
129 red boxes in Figure 1 are there only to draw attention to the MCR regions that are depicted  
130 by the orange and burgundy shading within the boxes. Climate data were averaged over  
131 these shaded MCR regions within the boxes. The MCRs are notably different in size with  
132 southwest southern Africa the smallest and the Mediterranean the largest.

#### 134 *b. Observational data*

135 For precipitation and temperature observations over land we use the latest data set  
136 from the University of East Anglia Climatic Research Unit CRU TS3.25 which provides  
137 data on a  $0.5^\circ$  grid at monthly resolution from 1901 to 2016 (Harris et al. 2014) accessed  
138 from <http://dx.doi.org/10.5285/c311c7948e8a47b299f8f9c7ae6cb9af>. For SST and  
139 200hPa heights we use data from the National Centers for Environmental Prediction-National  
140 Center for Atmospheric Research (NCEP-NCAR) Reanalysis (Kalnay et al. 1996; Kistler  
141 et al. 2001) for 1949 to 2016 accessed from [https://iridl.ldeo.columbia.edu/SOURCES/](https://iridl.ldeo.columbia.edu/SOURCES/.NOAA/.NCEP-NCAR/.CDAS-1/)  
142 [.NOAA/.NCEP-NCAR/.CDAS-1/](#). To assess if data limitation in the southern hemisphere prior

143 to the satellite era influences the results we also conducted the analyses for 1979 to 2016  
144 and found very similar results to those for 1949 to 2016 and hence just show results for  
145 the longer period. In addition we analyzed observed precipitation data from the Global  
146 Precipitation Climatology Center (GPCC) at half degree resolution covering 1901 to 2013  
147 (Schneider et al. 2011), accessed from [http://iridl.ldeo.columbia.edu/SOURCES/.WCRP/](http://iridl.ldeo.columbia.edu/SOURCES/.WCRP/.GCOS/.GPCC/.FDP/.version7/.0p5/)  
148 [.GCOS/.GPCC/.FDP/.version7/.0p5/](http://iridl.ldeo.columbia.edu/SOURCES/.WCRP/.GCOS/.GPCC/.FDP/.version7/.0p5/) and for the U.S. from the PRISM group at Oregon  
149 State University (Daly et al. 2008) (available at [www.prism.oregonstate.edu](http://www.prism.oregonstate.edu), accessed  
150 6/21/18).

151 *c. SST-forced atmosphere model simulations*

152 To examine SST-forced variability we use a 16 member ensemble of simulations of  
153 the NCAR Community Atmosphere Model 5.3 (see [http://www.cesm.ucar.edu/models/](http://www.cesm.ucar.edu/models/cesm1.2/cam/docs/ug5_3/ug.html#idm218596792640)  
154 [cesm1.2/cam/docs/ug5\\_3/ug.html#idm218596792640](http://www.cesm.ucar.edu/models/cesm1.2/cam/docs/ug5_3/ug.html#idm218596792640), CAM5.3) forced by Hadley Centre  
155 SST data HadISST1 (Rayner et al. 2003). Atmospheric trace gas contents were held fixed  
156 (mixing ratios are  $CO_2 = 3.55 \times 10^{-4}$ ,  $CH_4 = 1.71 \times 10^{-6}$ ,  $N_2O = 0.311 \times 10^{-6}$ ,  $F11 =$   
157  $0.28 \times 10^{-9}$ ,  $F12 = 0.503 \times 10^{-9}$ ). The 16 members are begun from different initial condi-  
158 tions on January 1 1856 such that the unforced variability in each member is uncorrelated  
159 with that in each other member. We analyze the mean across the ensemble members which  
160 isolates the SST-forced component of the atmosphere simulations common to all members.  
161 The simulations were generated at Lamont and run at T42 spectral resolution with 30 vertical  
162 hybrid-sigma levels.

163 *d. Radiatively-forced model simulations*

164 To examine climate change caused by external forcing, such as changes in the trace gas  
165 content of the atmosphere due to human activity, we use models from the Coupled Model  
166 Intercomparison Project Five (CMIP5, Taylor et al. (2012)). Since we conduct an analysis of  
167 the contributing terms to changes in precipitation we use all the models that make available  
168 all the data needed for evaluation of the moisture budget with sufficient vertical resolution  
169 to perform vertical integrals and at 6 hourly time intervals to allow evaluation of moisture

170 transports by transient eddies. These are the same 22 models as in Seager et al. (2014c).  
171 To create a multimodel ensemble mean we first evaluate the mean of ensemble members  
172 for each model using runs continuous between historical and future projections and then  
173 average across models. Thus each model receives equal weight in the multimodel ensemble  
174 mean despite different ensemble sizes for models. For the 1901 to 2005 period we use the  
175 historical all-forcings simulations and for 2006 to 2040 we use the RCP8.5 emissions scenario  
176 projections. All model data are regridded to a common  $1^\circ \times 1^\circ$  grid. The list of models,  
177 their origin and some details are provided in Table 1.

### 178 **3. Climatology and variability of climate for Mediterranean-** 179 **type climates**

#### 180 *a. Climatology*

181 To understand the large-scale dynamical context of MCRs we plot in Figure 2, for the  
182 November to February and May to August seasons, the land precipitation and sub-monthly  
183 200hPa meridional velocity variance, a common measure of the extratropical storm track  
184 (see, for example, Berberry and Vera (1996); Chang et al. (2002)), and sea level pressure.  
185 In winter, the location of the MCRs poleward of arid subtropical regions with, in North  
186 America and Europe, more humid regions on their poleward side, is clear and arises from their  
187 positioning in, or on the equatorward flank of, the mid-latitude storm track. The storm track  
188 provides the winter precipitation. In the summer, the mid-latitude storm track is weaker  
189 and further poleward and each MCR is on the eastern flank of the subtropical anticyclones  
190 and hence under equatorward flowing, descending air (Rodwell and Hoskins 2001; Seager  
191 et al. 2003a). This provides for the warm or hot and dry summers. The Mediterranean  
192 itself is under a ridge expanding eastward from the North Atlantic subtropical high that is  
193 likely connected to Asian monsoon-induced subsidence (Rodwell and Hoskins 1996, 2001;  
194 Simpson et al. 2015). The commonality of the MCRs in terms of the large-scale dynamics  
195 context is clear and establishes the broad similarity in these climates on five continents.

196 Figure 3 shows the climatological seasonal cycle of precipitation and temperature for the



197 six MCRs. The six MCRs have remarkably similar seasonal cycles: maximum precipitation  
198 in December-January (June-July) and minimum precipitation in July-August (December-  
199 January) in the northern (southern) hemisphere. The temperature seasonal cycles are sim-  
200 ilarly comparable: minimum temperature in December-January (June-August) and maxi-  
201 mum temperature in July-August (December-February) in the northern (southern) hemi-  
202 sphere. Absolute precipitation and temperature do, however, differ across MCRs. In order  
203 from wettest to driest precipitation maxima, the MCRs are: Pacific Northwest, Califor-  
204 nia, Chile, and then Mediterranean, southwest southern Africa and southwest Australia as  
205 a group. In order from warmest to coolest summer temperature maxima, the MCRs are:  
206 Mediteranean, southwest Australia, southwest southern Africa, California, Pacific North-  
207 west, Chile. Figure 1 also shows the annual mean precipitation which makes clear the  
208 variation in seasonal maximum precipitation is reflected in the variation of overall aridity  
209 with the Pacific coast MCRs being less arid than the Mediterranean, southern Africa and  
210 Australian MCRs.

211 Figure 3 also shows box and whiskers plots of the median, 25th and 75th percentile, the  
212  $\pm 2.7\sigma$  range and outliers (beyond  $\pm 2.7\sigma$  for a normal distribution) for the temporal distribu-  
213 tion of area mean precipitation for each month in each MCR. Again there is much similarity  
214 across MCRs. The summer dry season is a time of very little precipitation variability while  
215 the winter wet season has substantial variability. The size of the 25th to 75th percentile range  
216 typically equals a quarter to a third of the value of the monthly mean precipitation but the  
217 full range of monthly precipitation (excluding outliers) varies from next to no precipitation  
218 to twice the normal. The three northern hemisphere MCRs have maximum temperature  
219 variability during the wet season but in the southern hemisphere temperature variability  
220 is more evenly spread through the year. Although not investigated here, we suspect this  
221 inter-hemispheric difference is due to the large area of continents in the northern hemisphere  
222 that get cold in winter causing large land-sea and meridional temperature contrasts that  
223 circulation variability can translate into large amplitude temperature variability (Schneider  
224 et al. 2015).

225 *b. Interannual variability of winter precipitation*

226 1) OBSERVED RELATIONS

227 The seasonal cycles clearly suggest that variability of a four month winter season mean  
228 precipitation will be the dominant feature of interannual hydroclimate variability in MCRs  
229 with likely impacts on water resources, hydrology and ecosystems. For the northern hemi-  
230 sphere we define November through February, and for the southern hemisphere we define  
231 May through August, as four month averaged periods to analyze and for convenience refer  
232 to these as the winter seasons. It is recognized that such temporal averaging is rarely ideal  
233 since the phenomena that influence variability within the season and the seasonal cycle itself  
234 occur within a time continuum. Given their subtropical locations and exposure to winter  
235 storm tracks that can be displaced by tropically-forced teleconnections (e.g. Trenberth  
236 et al. (1998); Seager et al. (2003a)), it might be expected that each of the MCRs would be  
237 influenced to some degree by the dominant source of SST-forced interannual variability, the  
238 El Niño-Southern Oscillation (ENSO). Also, given their latitude, it might be expected that  
239 MCRs will be at the equatorward flank of variability induced by the northern and southern  
240 annular modes. In addition, other modes of SST-forced and internal variability could be  
241 important.

242 In Figure 4 we show the regression of winter mean 200hPa geopotential heights and  
243 SST on concurrent winter mean precipitation anomalies in the MCRs for the 1949 to 2016  
244 period covered by the NCEP-NCAR Reanalysis. To remove long term climate change, to be  
245 considered separately below, these analyses are conducted on data that have been linearly  
246 detrended. Despite the above expectation, only California and Chile show a connection of  
247 winter wetness to ENSO and only weakly so. The association is in the sense of El Niño (La  
248 Niña) winters tend to be wet (dry) but we know based on prior work (Seager et al. 2015;  
249 Jong et al. 2016) that the association for California is largely restricted to the El Niño-wet  
250 side.

251 Not only is the ENSO influence restricted to those MCRs that border the eastern Pacific  
252 Ocean, but this appears the only ocean influence on MCR winter precipitation variability. For  
253 the Pacific northwest, Mediterranean, southwest southern Africa and southwest Australia the

254 results show no regions with statistically significant SST anomalies that appear to be forcing  
255 precipitation variability. For the Pacific northwest the SST anomalies that do appear are  
256 consistent with forcing from the atmosphere in the form of cold/dry (warm/moist) advection  
257 generating enhanced (reduced) ocean to atmosphere surface heat flux and cool (warm) SST  
258 anomalies. The cool waters west of southwest Australia are also consistent with cooling due  
259 to enhanced westerlies. The height anomalies associated with southwest Southern Africa  
260 winter precipitation variability are similar to those previously noted by Reason et al. (2002).

261 The signal of the northern annular mode shows up clearly in relation to Mediterranean  
262 winter precipitation variability. Wet winters go along with a negative northern annular  
263 mode that would also be a negative North Atlantic Oscillation (NAO) with anomalous high  
264 heights over the subpolar North Atlantic and northern high latitudes and negative heights  
265 over the subtropical Atlantic and subtropical northern latitudes. The height anomalies  
266 are positioned so that during wet winters the Mediterranean region experiences enhanced  
267 westerly flow. Although the annular mode anomalies are hemispheric in scale, the dominant  
268 mode influencing winter precipitation variability in the Pacific Northwest is instead a North  
269 Pacific to North Atlantic wave train that places, during wet winters, strong westerlies over  
270 the region and which appears to arise from internal atmospheric variability. Any influence  
271 of the southern annular mode is not leading for any of the three southern hemisphere MCRs.  
272 Chile instead reflects an ENSO influence, and both southwest southern Africa and southwest  
273 Australia tend to have wet (dry) winters when local westerlies are strong (weak) with only  
274 southwest Australia having some hint of being related to annular mode of variability (and  
275 perhaps more to an Australian regional version of the Antarctic Oscillation as in Meneghini  
276 et al. (2007)).

277 These results are consistent with, or not inconsistent with, prior work on SST relations  
278 to precipitation variability in MCRs. Seager et al. (2015) review work on California winter  
279 precipitation variability and show that there is a weak correspondence of El Niño events to  
280 wet winters but no association between La Niña and dry winters. Garreaud et al. (2018) show  
281 an ENSO association to winter precipitation variability in Chile. This is consistent with the  
282 hemispherically symmetric aspects of ENSO-driven climate variability (Seager et al. 2003a)  
283 with the anomalies in Chile occurring in the northern summer (southern winter) before peak

284 ENSO events and the impact on California in the following northern winter. We have shown  
285 an association between the NAO and Mediterranean winter precipitation which has been long  
286 known (Hurrell 1995). Recently it has been claimed that the winter NAO is significantly  
287 driven by tropical SST variations (Scaife et al. 2014) but those SST-forced variations do not  
288 appear in our analysis due to the dominant internal atmospheric origin of NAO variability.  
289 For southwest southern Africa an apparent connection of ENSO to precipitation variability  
290 occurs in the dry season (Rowell 2013) and, while Philippon et al. (1985) claimed an  
291 ENSO connection to wet season precipitation variability during 1979 to 1999 for the wider  
292 southwest, this is actually weak in the MCR (see their Figure 5). The association of wet  
293 and dry winters in southwest Australia with anomalous westerlies and easterlies was noted  
294 by Allan and Haylock (1993) and Smith et al. (2000). An association of wet (dry) with  
295 La Niña (El Niño) is obscured in this analysis since it does not reach statistical significance  
296 which is consistent with the ENSO teleconnection to Australia being focused in the east of  
297 the continent and only weakly influencing the Australian MCR (Risbey et al. 2009). That  
298 the ENSO relation to the southern hemisphere MCRs is weak is consistent with O’Kane  
299 et al. (2017) who emphasize the importance of internal mid-latitude waveguide dynamics to  
300 circulation variability across the southern hemisphere.

## 301 2) MODEL-BASED ANALYSIS OF SST-FORCED PRECIPITATION VARIABILITY IN MCRS

302 Based on the results in the prior subsection we would not expect a high level of agreement  
303 between the observed time series of winter precipitation in MCRs and those simulated by  
304 SST-forced models. This is because the observational analysis does not identify a role for SST  
305 forcing other than in California and Chile where it is still, nonetheless, quite weak. Figure  
306 5 shows the observed and model ensemble mean time histories of winter precipitation and  
307 temperature for each MCR as well as, with shading, the spread across the model ensemble.  
308 In California, Chile and southwest Australia the ensemble mean precipitation time series is  
309 correlated with the observed history at the 5% statistical significance level (according to a  
310 two-sided t-test) but with correlation coefficients of 0.17, 0.42 and 0.19 respectively. Hence  
311 Chile is the only MCR where SST-forcing appears to explain more than 10% of the total

312 variance of winter precipitation.

313 The SST-forced climate model experiments allow further interrogation of the role for  
314 SST-forcing. The ensemble mean of the simulations closely identifies the SST-forced com-  
315 ponent common to each ensemble member. Figure 6 is as for Figure 4 but computed on the  
316 ensemble mean of the SST-forced simulations with CAM5.3. Here we use only the 1949 to  
317 2016 period of the model simulations to match the NCEP-NCAR period analyzed above.  
318 Here we uncover the maximum potential for the oceans to drive winter precipitation variabil-  
319 ity in the MCRs. For the Pacific northwest, La Niña conditions have a weak relation to wet  
320 winters. For both California and Chile there is a clear association in the SST-forced signal  
321 between El Niño and wet winters. The fact that this is less clear in the observational analysis  
322 is almost certainly due to the strength of internal atmosphere variability and its influence  
323 on precipitation in these regions. For the Mediterranean too, an ENSO influence is apparent  
324 consistent with Scaife et al. (2014), while Pozo-Vasquez et al. (2005, 2001) show the rela-  
325 tion is primarily La Niñas favoring a positive NAO and dry conditions across most of the  
326 Mediterranean. The ENSO-Mediterranean precipitation teleconnection may also vary over  
327 time due to the influence of other modes of variability and location of tropical Pacific SST  
328 anomalies (Lopez-Parages and Rodriguez-Fonseca 2012; Lopez-Parages et al. 2016). Signif-  
329 icant, however, is that here we find this SST-forced precipitation signal is weak compared  
330 to that of the NAO. Since the NAO is primarily a mode of internal atmosphere variabil-  
331 ity and only weakly SST-forced, these results are consistent with the observational analysis  
332 identifying internal atmosphere (NAO) variability, not SSTs, as the leading cause of winter  
333 precipitation variability in the Mediterranean. There is essentially no SST-forced signal over  
334 southwest southern Africa and the association between wet winters in southwest Australia  
335 and La Niña is consistent with Risbey et al. (2009) in both sign and weak amplitude.

336 The time series of observed winter precipitation in all the MCRs (Figure 5) show strong  
337 variability and any long term trends are weak in comparison but, close inspection, shows  
338 likely drying trends in the Mediterranean, Chile, southwest southern Africa and southwest  
339 Australia, which we examine in the next section. Warming trends appear clearly in the  
340 Mediterranean, Chile, southwest southern Africa and southwest Australia. The trends are  
341 faithfully reproduced by the SST-forced model but it is also notable that the interannual

342 variability of surface temperature is too (numbers in parentheses show correlation coefficients  
343 for detrended time series). Further examination, not shown here, shows this to be of little  
344 interest because warm anomalies are caused by circulation anomalies that also warm the  
345 waters offshore from the MCRs. When these warm water anomalies are imposed in the model  
346 it causes a warm response in the MCRs even though the responsible circulation anomalies  
347 are not simulated, i.e. the right answer for the wrong reason.

## 348 **4. Long term change in precipitation in Mediterranean-** 349 **climate regions**

### 350 *a. Observed and modeled trends over the past century*

351 Figure 7 shows the linear trend in land precipitation over 1901 to 2016 that was removed  
352 before conducting the analyses shown in the previous section. In both California and the  
353 Pacific Northwest the trend within the MCR is spatially variable. In contrast, there has been  
354 widespread drying across Chile, southwest Australia and the Mediterranean, except Iberia.  
355 In the very small MCR of southwest southern Africa there has also been drying. Figure 8  
356 shows the multimodel mean trend over the same period in the CMIP5 models. This bears  
357 notable similarity to the observed trend. In the models, of the six MCRs only the west  
358 coast of North America has got wetter while the other four have dried. The spatial patterns  
359 in which the MCR precipitation change occurs are also similar between observations and  
360 model response to external forcing. In North America this is widespread wetting over the  
361 US but drying in western Mexico. In the Mediterranean region observations and models  
362 agree on drying across North Africa and around the north shores of the Mediterranean Sea.  
363 In Australia there is agreement on drying of all of southwest Australia not just the MCR.  
364 There is disagreement in South America with the models suggesting wetting south of the  
365 Chile MCR but the observations extending the drying into the humid region to the south. In  
366 Africa the models are more emphatic in drying all of southern Africa. Nonetheless, given the  
367 strength of natural variability, uncertainties in the observational data and potential model  
368 errors and biases, this comparison is suggestive that each of the MCRs is already experiencing

369 forced and human-induced precipitation change.

370 The lower panel of Figure 8 shows box and whiskers plots of the distribution of trends  
371 across the CMIP5 model ensemble. The median is plotted as the horizontal line across the  
372 box and the upper and lower limits of the box are the 25th and 75th percentiles of the dis-  
373 tribution across models, the range is shown by the whiskers, outliers by red crosses and the  
374 mean by a black asterisk. It is striking that for the Mediterranean, Chile, southwest southern  
375 Africa and southwest Australia the model ensemble spread is predominantly drying, further  
376 indicating the robustness of this human-induced climate change signal. In this panel we  
377 also show the trends from the CRU and GPCP observational data and both show drying  
378 indicating a large degree of model-observations agreement on aridification. The model en-  
379 semble indicates wetting for California and a wet tendency for the Pacific northwest. Both  
380 are on the wet side of the observational trends (including PRISM) which are close to neutral.  
381 While much southern hemisphere climate change over recent decades has been attributed to  
382 ozone depletion that is for the summer half year when stratospheric ozone can absorb solar  
383 radiation (e.g. Polvani et al. (2011)). In the winter season, ozone depletion is unlikely to be  
384 influential (Thompson et al. 2011; Franzke et al. 2015) and the radiatively-forced changes  
385 arise instead from the increase in GHGs.

386 Models agree that the MCRs of the Mediterranean, Chile, southwest southern Africa  
387 and southwest Australia should be drying and the observations in these MCRs do indeed  
388 show drying. By using a bootstrapping methodology on the observed data we can assess  
389 the probability that these four MCRs would have simultaneously dried, to the degree seen  
390 in observations, through the chance sampling of interannual variability alone. All corre-  
391 lations of the interannual variability between these four regions are less than 0.06 and no  
392 regions have significant autocorrelation in precipitation from one year to the next except for  
393 southwest Australia where it is reduced to insignificant values when the century long trend  
394 is removed. The lack of autocorrelation of the interannual variability means it is appropri-  
395 ate to compare the observed trends to the distribution of trends obtained from time series  
396 constructed by randomly selecting individual years (with replacement) from the observed  
397 record. The probability of obtaining the observed magnitude of trends by chance are 9.3%  
398 for the Mediterranean, 5.2% for Chile and 26.7% for southwest southern Africa and essen-

399 tially zero for southwest Australia. For the regions other than southwest Australia, while  
400 individually they have not dried significantly more than expected from the sampling of in-  
401 terannual variability at the 5% level, the chances of obtaining a simultaneous drying of these  
402 three regions of the magnitudes observed, given their independence, is only around 0.1%  
403 i.e.,  $p = 0.093 \times 0.052 \times 0.267$ . These statistical analyses raise confidence that the observed  
404 drying in the four MCRs where models simulate drying would not have arisen from internal  
405 climate variability alone and that external forcings have made an important contribution.

406 *b. Model projections of near term future change in the hydrological cycle over Mediterranean-*  
407 *type climates and the physical causes*

408 Here we use the CMIP5 models to determine the winter hydroclimate change they project  
409 for the coming decades and the mechanisms responsible. First in Figure 9 we show the model  
410 agreement on sign of winter precipitation change for 2021-2040 relative to 1979-2005 (the  
411 same near-term future and recent past periods used by Seager et al. (2014b,c)). The models  
412 project all MCRs except in North America to continue to dry in coming decades and this is  
413 robust (more than three quarters of models agree on the sign of the change and agree with  
414 the ensemble mean change) for all of the drying MCRs. Together with the ability of the  
415 CMIP5 models to simulate historical drying this raises confidence that the changes to be  
416 discussed are robust projections of the models.

417 To examine mechanisms of hydroclimate change we use a moisture budget breakdown  
418 methodology as in Seager et al. (2010, 2014b,c) using the “best-practises” methods of  
419 Seager and Henderson (2013). We divide all quantities into monthly means, represented  
420 by overbars and departures from monthly means, represented by primes with climatological  
421 monthly means denoted by double overbars. Then the vertically integrated moisture budget,  
422 written with model layer indicated by  $k$  and  $K$  the total number of levels, can be rewritten



423 as:

$$\Delta \overline{\overline{P}} - \Delta \overline{\overline{E}} \approx -\frac{1}{g\rho_w} \nabla \cdot \sum_{k=1}^K \Delta(\overline{\overline{\mathbf{u}_k \bar{q}_k dp_k}}) - \frac{1}{g\rho_w} \nabla \cdot \sum_{k=1}^K \Delta(\overline{\overline{\mathbf{u}'_k q'_k dp_k}}), \quad (1)$$

$$\begin{aligned} &\approx -\frac{1}{g\rho_w} \sum_{k=1}^K \Delta(\overline{\overline{(\mathbf{u}_k \cdot \nabla \bar{q}_k) dp_k}}) - \frac{1}{g\rho_w} \sum_{k=1}^K \Delta(\overline{\overline{\bar{q}_k \nabla \cdot \mathbf{u}_k dp_k}}) \\ &\quad - \frac{1}{g\rho_w} \nabla \cdot \sum_{k=1}^K \Delta(\overline{\overline{\mathbf{u}'_k q'_k dp_k}}) - \frac{1}{g\rho_w} \Delta(\overline{\overline{q_s \mathbf{u}_s \cdot \nabla p_s}}). \end{aligned} \quad (2)$$

424 Here  $\Delta(\cdot)$  indicates change from an average over one period to an average over another  
 425 period,  $P$  is precipitation,  $E$  is evaporation (taken to include transpiration),  $g$  is the accel-  
 426 eration due to gravity,  $\rho_w$  is the density of water,  $p$  is pressure,  $q$  is specific humidity and  
 427  $\mathbf{u}$  the vector horizontal velocity. The first and second terms on the right of Eq. 1 are the  
 428 moisture convergence by the mean flow and submonthly transient eddies, respectively. The  
 429 approximation in Eq. 1 comes from neglecting time rate of change of moisture (which is  
 430 small compared to the other terms) and ignoring terms involving  $dp'_k$  which is acceptable  
 431 (see Seager and Henderson (2013))). In Eq. 2 the change in mean flow moisture convergence  
 432 has been broken down into components. The first involves the change in moisture advection,  
 433 i.e. flow across spatial gradients of moisture. The second involves change in moisture con-  
 434 vergence related to the divergent flow. This is primarily influenced by mass divergence or  
 435 convergence in the lower levels where moisture is concentrated. The third (the fourth term  
 436 on right hand side) is a surface term that arises from bringing the divergence operator inside  
 437 the vertical integral in order to enable the separation into advection and mass divergence  
 438 terms.

439 The moisture budget change can be further decomposed into terms related to (i) changes  
 440 in humidity with unchanged circulation and (ii) changes in circulation with unchanged hu-  
 441 midity. The terms related to the moisture advection and the mass divergent flow can be  
 442 approximated as:

$$-\frac{1}{g\rho_w} \sum_{k=1}^K \Delta(\overline{\overline{(\mathbf{u}_k \cdot \nabla \bar{q}_k) dp_k}}) \approx -\frac{1}{g\rho_w} \sum_{k=1}^K \overline{\overline{\mathbf{u}_{k,20}}} \cdot \Delta(\overline{\overline{\nabla \bar{q}_k dp_k}}) - \frac{1}{g\rho_w} \sum_{k=1}^K \nabla \bar{q}_{k,20} \cdot \Delta(\overline{\overline{\mathbf{u}_k dp_k}}), \quad (3)$$

$$-\frac{1}{g\rho_w} \sum_{k=1}^K \Delta(\overline{\overline{\bar{q}_k \nabla \cdot \mathbf{u}_k dp_k}}) \approx -\frac{1}{g\rho_w} \sum_{k=1}^K \Delta(\overline{\overline{\bar{q}_k dp_k}}) \nabla \cdot \overline{\overline{\mathbf{u}_{k,20}}} - \frac{1}{g\rho_w} \sum_{k=1}^K \bar{q}_{k,20} \Delta(\overline{\overline{\nabla \cdot \mathbf{u}_k dp_k}}). \quad (4)$$

443 Further approximation comes from ignoring terms quadratic in  $\Delta$ , covariances of anomalous  
444 monthly means and from using the 1979 to 2005 values for  $dp_k$ . In Eqs. 3 and 4 the  
445 first terms on the right are referred to as the ‘thermodynamic terms’ since they involve the  
446 changes in humidity while the circulation is fixed and the second terms are referred to as the  
447 ‘mean circulation dynamics’ terms since they involve the changes in the circulation while the  
448 humidity is fixed. The thermodynamic term is, however, not solely thermodynamic since  
449 the humidity field itself can change due to circulation change, not just temperature change.

450 The computation was carried out exactly as in Seager and Henderson (2013) to which  
451 the reader is referred to for more details. Briefly, 6-hourly data are used to compute the  
452 transient moisture fluxes and monthly mean data to compute the monthly mean moisture  
453 fluxes. In the vertical integral monthly mean pressure thicknesses are used. Derivatives  
454 are computed using second order centered differences and accounting for uneven grids. The  
455 vertical integration extends to the surface pressure. The pressure thickness for this lowest  
456 layer equals the surface pressure minus the pressure of the lowest reported level and the  
457 velocities and humidity assigned to the layer are those of the lowest reported pressure level.

458 Figures 10-13 show the changes in  $P$ ,  $E$ ,  $P - E$ , mean flow moisture convergence, the  
459 advection and mass divergence contributions to mean flow moisture convergence, the surface  
460 term and transient eddy moisture convergence for the 2021-2040 winter average minus the  
461 1979 to 2005 winter average. Over North America (Figure 10) the MCR is projected to  
462 experience an increase in winter  $P$  but, because of warming and higher evaporative demand,  
463 its southern extent is projected to see a decrease in  $P - E$ . Transient eddy moisture con-  
464 vergence is projected to decrease across the MCR (a consequence of weaker eddies in the  
465 lower troposphere, see Seager et al. (2014c)). Increased mean flow moisture convergence  
466 provides the wetting with both the advection and mass divergence terms important. Prior  
467 work (Seager et al. 2014c; Simpson et al. 2016) has shown that this is partly thermodynamic  
468 (the MCR region is wet in winter and rising humidity in a warmer atmosphere makes it wet-  
469 ter) and partly due to adjustment of the stationary wave field creating a trough offshore and  
470 southwesterly winds into the MCR.

471 Widespread declines of  $P$  and  $P - E$  are projected for the Mediterranean (Figure 11) and  
472 are largely driven by a move towards mean flow moisture divergence and the term involving

473 the mass divergence being key. As also shown before (Seager et al. 2014b; Zappa et al.  
474 2015), this is related to a move towards a ridge in the region that again is linked to an  
475 adjustment in the planetary scale stationary wave field, but of unknown origin.

476 For South America, southern Africa and Australia (Figures 12 and 13) the models project  
477 drying (for both  $P$  and  $P - E$ ) for the MCR regions driven by mean flow moisture divergence.  
478 In Chile the mass divergence term contributes drying for the southern part of the MCR but  
479 moisture advection is a drying term across the MCR. For the MCRs of southern Africa and  
480 Australia it is also the advection term that drives consistent drying. In all three southern  
481 hemisphere MCRs, transient eddy moisture divergence acts reactively and diffusively to  
482 provide a wetting tendency offsetting mean flow induced drying.

483 To assess whether these changes arises from change in the flow or the moisture field we  
484 examined the further moisture budget decomposition in Eqs. 3 and 4 and this is shown  
485 for the southern hemisphere in Figures 14 and 15. Dynamic terms are on the left and  
486 thermodynamic terms on the right. The thermodynamic term most closely related to the  
487 “wet-get-wetter” paradigm - increasing humidity in a region of low-level mass convergence  
488 (upper right) - does provide a wetting tendency in the Chile and southwest Australia MCRs  
489 (but less so in southwest southern Africa) but this is overwhelmed by a thermodynamic  
490 drying tendency due to increased drying by advection (lower right). There is also a dynamic  
491 drying tendency due to a shift towards increased low-level mass divergence in the MCR region  
492 (upper left). The moisture budget change is very similar in the MCRs of southern Africa  
493 and Australia: the thermodynamic mass convergence term provides a wetting tendency that  
494 is overwhelmed by i) thermodynamic drying due to increased dry advection and ii) dynamic  
495 drying due to increased low level mass divergence.

496 Next we investigate the causes of these thermodynamical and dynamical changes. In  
497 Figure 16 we show for the southern hemisphere the climatology of, and change in, humid-  
498 ity vertically-integrated from the surface to 600hPa and the 850hPa winds. The southern  
499 hemisphere MCRs sit within widespread subtropical minima of the increase in vertically  
500 integrated humidity. Although not shown here, computations as in Ting et al. (2018), show  
501 that this subtropical minima is associated with a reduction in relative humidity in the lower  
502 troposphere above the boundary layer. Declining free troposphere relative humidity in the

503 subtropics to mid-latitude region under global warming has long been noted and is explained  
504 in terms of (i) the poleward expansion of the Hadley Cell and (ii) smaller temperature in-  
505 creases in the upper level regions where the air was last saturated than in the regions to  
506 which the air descends (Lorenz and DeWeaver 2007; Sherwood et al. 2010; O’Gorman and  
507 Muller 2010; Wright et al. 2010; Lau and Kim 2015).

508 Within these subtropical regions, the humidity increase is locally minimized in the MCRs.  
509 The wind changes show a clear trend to easterlies north of  $40^{\circ}S$  (east Pacific) and  $35^{\circ}S$   
510 (Indian Ocean) and towards westerlies to the south. Comparing to the climatological state  
511 (Figure 15, top panel), these changes represent a poleward expansion of the Hadley Cell and  
512 trade winds and a poleward shift and intensification of the extratropical westerlies. Westerly  
513 winds impinging on the coast create convergence because of topography and increased surface  
514 friction. Hence, in the region of easterly wind change, there is a shift towards low level mass  
515 divergence and, consequently, subsidence off the coasts of the MCRs, causing a reduction in  
516 specific humidity via moisture divergence. Since this process creates a local specific humidity  
517 change minimum right at and west of the coast, the moisture advection term that combines  
518 the unchanged westerly flow with the changed humidity field is a drying term for the MCRs  
519 inland. While that advection term is a thermodynamic term it should be recognized that the  
520 separation is not clean because, as mentioned, the pattern of humidity change is influenced  
521 by the circulation change.

## 522 5. Discussion

523 The Koppen climate classification is based entirely on long term climatological properties  
524 of a region and pays no attention to variability of climate and uses three letters for char-  
525 acterization. Mediterranean-type climate are identified as being temperate ( $C$ ), with a dry  
526 summer ( $s$ ) and hot ( $a$ ) or warm ( $b$ ) summers, hence both  $Csa$  and  $Csb$  climates. Despite the  
527 absence of attention to climate dynamics, the scheme successfully identifies Mediterranean-  
528 type climate regions on five continents that do share commonalities in climate, geographical  
529 locations and planetary-scale dynamical context.

530 As we have shown, the MCRs also have similar climatologies of precipitation and tem-

531 perature variability. However the causes of variability differ across the MCRs. It might be  
532 expected that given their subtropical to mid-latitude location each MCR would be subject  
533 to variability driven from the tropics and via annular modes. However, tropically-forced  
534 variability primarily arises from the Pacific and, hence, it is not surprising that the North  
535 American west coast and Chile are the prime recipients of its induced variability. Although  
536 ENSO-induced variability is global, the other MCRs are in locations remote from the tropi-  
537 cal Pacific and/or near nodal lines in ENSO-teleconnections (the Mediterranean, southwest  
538 Southern Africa, southwest Australia) (Garreaud and Battisti 1999). In addition, in the  
539 southern hemisphere, the winter (analyzed here) is a season of growing or decaying, but not  
540 peak, ENSO variability which limits the strength of tropical forcing of circulation variabil-  
541 ity (O’Kane et al. 2017). This is consistent with the ENSO-signal in the southern Africa  
542 and Australian MCRs remaining weak in analysis of the SST-forced model ensemble mean  
543 even though that isolates the SST-forced signal by averaging over internal variability. In  
544 all MCRs the dominant source of variability appears to be internal atmosphere variability.  
545 This is understandable given their location at the equatorward flank of mid-latitude storm  
546 tracks (Hoskins and Valdes 1990; Trenberth 1991) that allow for considerable internally-  
547 generated variability (O’Kane et al. 2017). Hence, even for the ENSO-teleconnected MCRs  
548 at the western coast of the Americas, the ocean-forced signal is weak relative to internal at-  
549 mospheric variability. Of other modes of ocean-related variability, the Indian Ocean Dipole  
550 Mode does influence Australian climate but the influence is weak over the MCR in the south-  
551 west (Risbey et al. 2009). The minor role for ocean forcing means that predictability of  
552 interannual variability of winter precipitation in the MCRs will largely be small beyond the  
553 timescale of numerical weather prediction based on initial conditions.

554 The annular modes are one major source of internal atmosphere variability in the extra-  
555 tropics and given their hemispheric inclusivity might be expected to influence the MCRs.  
556 However, only in the Mediterranean is the interannual variability of winter precipitation  
557 dominated by annular mode variability, also interpretable here as the NAO. As shown in  
558 Thompson and Wallace (2000) (see their Figure 1), the northern and southern annular modes  
559 variability lies somewhat poleward of the MCRs and their zonal structure is such that the  
560 Mediterranean is the only MCR that is located where there is substantial annular mode

561 variability.

562 There is commonality across the MCRs, with the exception of California, in trends over  
563 the past century towards drier winters. This is quite consistent with CMIP5 model sim-  
564 ulations and is likely a consequence of human-driven climate change (Polade et al. 2017;  
565 Delworth and Zeng 2014). The CMIP5 models project continuation of the historical trends.  
566 The mechanisms for this can be discussed in terms of three commonly used concepts of  
567 GHG-driven hydroclimate change, and one less commonly used.

568 *a. “Wet get wetter, dry get drier”*

569 The expectation is that as the atmosphere warms and can hold more water, those wet  
570 areas where moisture converges will become wetter as the atmosphere converges more mois-  
571 ture and vice versa for dry areas of moisture divergence (Chou and Neelin 2004; Held and  
572 Soden 2006). Since in winter, MCRs are regions of moisture convergence and wet, if this  
573 mechanism was dominant we would expect the MCRs to get wetter in winter. The moisture  
574 budget analyses do show that this thermodynamics term creates a wetting tendency. How-  
575 ever it is overwhelmed by other drying terms in all MCRs other than the North American  
576 west coast and hence “wet-get-wetter” is not a good guide for hydroclimate change in MCRs.

577 *b. Expansion of the Hadley Cell and tropics*

578 Lu et al. (2007) noted that global warming causes the Hadley Cell to expand as thermal  
579 stratification in the subtropics increases and moves the latitude at which the zonal flow  
580 becomes baroclinically unstable poleward. This would be expected to move the subtropical  
581 dry zones, which are under the descending branch of the winter hemisphere Hadley Cell,  
582 poleward, encroaching, at the west coast of continents, into the MCRs (see Grise et al.  
583 (2019) for a recent review of the character and causes of recent tropical expansion). The  
584 analysis shows that Hadley Cell expansion in the southern hemisphere (Feitas et al. 2017)  
585 is indeed a good way to think of the ongoing and model projected increase in aridity within  
586 the MCRs. The low level wind changes clearly show a poleward migration of the subtropical  
587 high pressure zones under the descending branch of the Hadley Cell and there is a zonal band

588 of decreasing precipitation at this latitude. The Hadley Cell is by definition a zonal mean  
589 phenomenon although the physical phenomenon of rising air in the tropics and descending air  
590 in the subtropics need not be zonally uniform and changes in the characteristics of these rising  
591 and descending regions may contribute to some zonally asymmetric changes. In contrast, in  
592 the northern hemisphere the greatly differing hydroclimate responses in California (wetting  
593 or little change) and the Mediterranean (strong drying) make explanation in terms only of  
594 Hadley Cell expansion inadequate and require an appeal to changes in zonally asymmetric  
595 stationary waves.

596 *c. Poleward shift of the mid-latitude westerlies and storm tracks*

597 Yin (2005) noted that global warming causes a poleward and upward shift of the storm  
598 tracks and an associated poleward movement of the jets and a move towards a high index  
599 state of the northern and southern annular modes. This change is part and parcel of the  
600 Hadley Cell expansion given the coupling between the axisymmetric tropical flow, the mid-  
601 latitude eddies and the jet streams (see, for example, Schneider (2006)). Our analyses here  
602 clearly show a projected poleward movement of the southern hemisphere winter westerlies  
603 which occurs owing to both the direct effect of  $CO_2$  increase and SST warming (Grise and  
604 Polvani 2011). Within the southern MCRs this reduces the westerlies, leading to anoma-  
605 lous easterly flow and divergence, subsidence, reduced humidity and precipitation. In the  
606 northern hemisphere prior work has again made clear the situation is more complex. At  
607 the location of the North American MCRs, the westerlies actually shift equatorward in the  
608 model projections (Simpson et al. 2014, 2016) but over the Mediterranean-Europe sector the  
609 westerlies do not so much shift in latitude as extend eastward into northern Europe which  
610 has the effect of placing high pressure over the MCR to the south (Woollings and Black-  
611 burn 2012; Simpson et al. 2014). Hence, viewing the drying of MCRs in terms of poleward  
612 movement of the mid-latitude circulation is also valid for the southern hemisphere but not  
613 the northern hemisphere without qualification.

614 *d. Changes in stationary waves*

615 Due to the large continents and high, broad, mountain chains the stationary wave field  
616 in the northern hemisphere has a larger amplitude than that in the southern hemisphere. In  
617 the southern hemisphere, changes in the stationary wave field do not need to be invoked to  
618 explain the hydroclimate change in MCRs and, instead, a more zonally symmetric view in  
619 terms of the Hadley Cell and an extratropical jet stream and storm track seems adequate.  
620 That said, intensification of drying in the MCRs does arise from local interactions between  
621 the continents and the zonal mean circulation shifts. In contrast, in the northern hemisphere,  
622 changes in the stationary waves have a powerful influence on winter hydroclimate change  
623 in the MCRs. Lengthening of the zonal scale of the stationary waves that are trapped in  
624 the subtropical-midlatitude wave guide in response to subtropical westerly strengthening  
625 (according to  $k \approx (\beta/\bar{u})^{1/2}$ , where  $k$  is zonal wavenumber,  $\beta$  is the meridional gradient of  
626 the Coriolis parameter and  $\bar{u}$  is the zonal mean zonal wind, for a uniform zonal flow and  
627 waves with large meridional scale), places southerly anomalies at the North American west  
628 coast that provide a wetting tendency (Simpson et al. 2016). The contrasting strong drying  
629 of the Mediterranean is also related to a stationary wave response and local high pressure  
630 (Seager et al. 2014b; Zappa et al. 2015) south of the eastward extended North Atlantic jet  
631 although the dynamics are not fully understood yet.

632 **6. Conclusions**

633 We have examined climate variability and change in the Mediterranean-type climate  
634 regions on five continents. Conclusions are as follows.

- 635 • The MCRs are justifiably grouped as climate types in that they have similar seasonal  
636 cycles of precipitation, temperature and variability. They also share commonality in the  
637 geographic location with reference to planetary scale dynamics. In the winter the west  
638 coast location ensures a temperate winter climate, free of continental cold air incursions  
639 and being within, or on the equatorward flank of, extratropical stormtracks makes the  
640 winters wet. The west coast location also ensures that in summer they are under the



641 equatorward flowing, descending branch of the subtropical anticyclones ensuring dry  
642 and warm or hot summers. The location between arid regions equatorward and more  
643 humid regions poleward ensures sizable winter season precipitation variability in all  
644 the MCRs.

- 645 • Despite the commonalities of climatology, the sources of interannual variability of win-  
646 ter precipitation vary notably across MCRs. Both California and Chile have modest  
647 influence from ENSO with El Niño favoring wet winters which is explainable in terms  
648 of them being downstream in the Rossby wave propagation path that originates in  
649 the equatorial Pacific deep convection anomalies driven by ENSO SST anomalies. A  
650 strong influence of annular mode variability is restricted to the Mediterranean where  
651 it is synonymous with North Atlantic Oscillation variability. For southwest southern  
652 Africa and southwest Australia, winter precipitation variability is most clearly related  
653 to the strength of local westerlies. In all regions, SST-forced models do uncover some  
654 SST-induced variability but it is weak compared to internal atmospheric variability  
655 indicating that seasonal prediction will have at best modest skill in the MCRs.
- 656 • All MCRs except in North America (California, Pacific Northwest) have experienced  
657 notable drying over the 1901 to 2016 period which reaches statistical significance at the  
658 5% level in many parts of the MCRs. Drying of the four MCRs outside North Amer-  
659 ica is highly unlikely to have occurred by chance sampling of interannual variability.  
660 This drying is also simulated in the historical simulations of the CMIP5 multimodel  
661 ensemble. These results strongly suggest that changes in radiative forcing contributed  
662 to the drying of MCRs outside North America.
- 663 • The CMIP5 models project a continuation of past trends into the near term future  
664 with, for the coming two decade period, reductions of winter precipitation in all MCRs  
665 other than the west coast of North America. The strong Mediterranean drying and  
666 lack of North American west coast drying have been previously explained in terms of  
667 changes in stationary waves that create important zonal asymmetries in climate change.  
668 For the three southern MCRs, all share common dynamical mechanisms of drying in  
669 terms of mean circulation change. First, Hadley Cell expansion and a poleward shift

670 of the westerlies create easterly wind anomalies at the location of the MCRs. Since  
671 prevailing westerlies, due to friction and topography, create moisture convergence in the  
672 MCRs, the easterly shift weakens this phenomena and induces drying. Second, there  
673 is a mixed dynamic-thermodynamic drying because models project coastal minima in  
674 specific humidity change at the MCRs and that allows prevailing westerlies to increase  
675 dry advection into the MCRs inland.

676 The ongoing climate change and future change, if it follows the model projections, will  
677 transform and move Mediterranean-type climate regions (Rubel and Kottek 2010). At  
678 the core latitudes of the regions, aridity will increase as winters become drier and temper-  
679 atures increase throughout the year. On the equatorward flanks some locations that are  
680 currently Mediterranean-type climates are likely to transition into subtropical desert or sub-  
681 tropical steppe. Examples of this possible transition are southern California, coastal North  
682 Africa and north-central Chile. Although it needs to be quantified, it appears plausible  
683 that encroachment of subtropical aridity might mean that southern Africa and southwest  
684 Australia lose their Mediteranean-type climate regions entirely. On the poleward flanks,  
685 Mediterranean-type climate regions on the North American west coast, Chile and Iberia will  
686 move into regions that currently have the marine, cool summer climate classification. Since  
687 the vegetation in Mediterranean-type climate regions is very closely related to the climate,  
688 it would be expected that these ongoing changes will be matched, with some delay, by eco-  
689 logical transformation too. These suspected changes are consistent with projected changes  
690 in the Koppen-Geiger climate classification done by Rubel and Kottek (2010) based on ear-  
691 lier climate projections and they show the southern Africa and southwest Australia MCRs  
692 to greatly shrink but not to entirely disappear. Of relevance for the west coast of North  
693 America is that, while the CMIP5 models project no drying for mid winter, they do robustly  
694 project drying (reduced  $P - E$ ) for late winter (Gao et al. 2014; Ting et al. 2018). From  
695 the direct human point of view, water resources in these regions will become increasingly  
696 strained. Ongoing year-to-year variability, if it maintains the historical amplitude, will occur  
697 against a drying mean climate so that droughts of unprecedented severity are increasingly  
698 likely to occur while the wet winters become not so wet and offer less relief. Given the  
699 lack of, or weak, predictability of winter climate in the Mediterranean-type climate regions

700 this offers the likelihood of the inevitable surprises of unpredicted and unprecedented serious  
701 drought. Adaptation methods based on probability assessments are already timely in each of  
702 the Mediterranean-type climate regions to plan for increasing aridity and the transformation  
703 of climate and ecosystems.

704 *Acknowledgments.*

705 This work was supported by NSF awards AGS 1734760, 1602581 and 1243204. TJO was  
706 supported by the Belmont Forum/JPI-Climate project INTEGRATE (NERC NE/P006809/1).  
707 We thank Giuseppe Zappa, Adam Scaife and Rene Garreaud for useful conversations, Naomi  
708 Henderson for essential work with the CMIP5 data base, moisture budgets and model simula-  
709 tions and Dong-Eun Lee for performing the CAM5.3 simulations, three anonymous reviewers  
710 and James Risbey for constructive criticism. RS would like to thank the staff and faculty of  
711 the Climatic Research Unit and School of the Environmental Sciences of the University of  
712 East Anglia for their great conviviality and support during an extended stay in spring 2018  
713 when much of this work was done, and the Lamont Doherty Earth Observatory for making  
714 the visit possible.

715 **7. Appendix**

716 In Figures 7 and 8 we compared the observed and CMIP5 multimodel mean trends in  
717 winter precipitation over 1901 to 2016 and argued that observed trends were consistent with  
718 those expected in response to changes in radiative forcing. In the analysis of future climate  
719 change, however, we examine differences between two decade long periods. For consistency, in  
720 Figure A1 we show the observed and CMIP5 multimodel mean change in winter precipitation  
721 for the recent historical period using 1997 to 2016 minus 1971 to 1990. For the MCRs the  
722 most recent two decade period has been drier in the eastern and western Mediterranean and  
723 over much of North Africa, Chile (other than a region south of Santiago), southwest South  
724 Africa and southwest Australia. At the North American coast the recent two decade period  
725 has been drier in Washington and Mexico but wetter in northern California and Oregon.

726 The CMIP5 multimodel mean has drying across much of the Mediterranean and in all the  
727 southern hemisphere MCRs though typically with lesser amplitude than observed. For these  
728 four MCRs there therefore is qualitative agreement between recent decadal timescale change  
729 and that predicted by models to occur due to changes in radiative forcing. Observed and  
730 modeled changes are also consistent in having no systematic change across the west coast of  
731 North America, the one MCR not predicted to dry in the future. As expected given this early  
732 stage in the climate system response to radiative forcing, only in some areas of the MCRs do  
733 the observed changes reach modest levels of statistical significance, while only in Chile and  
734 southwest Australia is there extensive model agreement on radiatively-forced drying across  
735 the MCR. We do not expect observed and modeled decadal timescale differences over the  
736 recent historical period to be particularly comparable given that the former will be influenced  
737 by modes of natural decadal variability and random sampling of interannual and internal  
738 atmospheric variability. Nonetheless, the limited qualitative agreement between observed  
739 and modeled differences provides evidence, additional to that provided by comparison of the  
740 116 year long trends, that the CMIP5 model ensemble is correctly simulating the response of  
741 winter precipitation in the MCRs to radiative forcing. Analyzing the physical mechanisms  
742 of observed change over the historical period, as done for models in Section 4, is not possible  
743 given the spurious trends and discontinuities in reanalyses introduced by changes in observing  
744 systems and data coverage that effect both hydrological quantities (e.g. Trenberth et al.  
745 (2011)) and measures of circulation (e.g. Grise et al. (2019)).

746

## 747 REFERENCES

- 748 Allan, R. J. and M. R. Haylock, 1993: Circulation features associated with the winter rainfall  
749 decrease in southwestern Australia. *J. Climate*, **6**, 1356–1367.
- 750 Aschmann, H., 1973: Distribution and peculiarity of Mediterranean ecosystems. *Mediterranean Type Ecosystems: Origin and Structure*, F. di Castri and H. A. Mooney, Eds.,  
751 Springer-Verlag, Berlin, 11–19.
- 752

- 753 Baich-Faig, A., et al., 2011: Mediterranean diet pyramid today. Science and cultural update.  
754 *Public Health Nutrition*, **14**, 2274–2284.
- 755 Berberry, E. H. and C. S. Vera, 1996: Characteristics of the southern hemisphere winter  
756 storm track with filtered and unfiltered data. *J. Atmos. Sci.*, **53**, 468–481.
- 757 Bowman, D. M. J. S., G. J. Williamson, J. T. Abatzoglou, C. A. Kolden, M. A. Cochrane,  
758 and A. M. S. Smith, 2017: Human exposure and sensitivity to globally extreme wildfire  
759 events. *Nature Ecol. Evol.*, **1**, 0058,doi:10.1038/s41559-016-0058.
- 760 Campins, J., A. Genoves, M. A. Picornell, and A. Jansa, 2011: Climatology of Mediterranean  
761 cyclones using the ERA-40 dataset. *Int. J. Climatol.*, **31**, 1596–1614.
- 762 Chang, E. K. M., S. Lee, and K. L. Swanson, 2002: Storm track dynamics. *J. Climate*, **15**,  
763 2163–2183.
- 764 Chou, C. and J. D. Neelin, 2004: Mechanisms of global warming impacts on regional tropical  
765 precipitation. *J. Climate*, **17**, 2688–2701.
- 766 Cook, B., J. E. Smerdon, R. Seager, and S. Coats, 2014: Global warming and drought in  
767 the 21st Century. *Clim. Dyn.*, DOI 10.1007/s00382-014-2075-y.
- 768 Cook, B. I., K. J. Anchukaitis, R. Touchan, D. M. Meko, and E. R. Cook, 2016: Spatiotem-  
769 poral drought variability in the Mediterranean over the last 900 years. *J. Geophys. Res.*,  
770 **121**, 2060–2074.
- 771 Daly, C., M. Halbleib, J. I. Smith, W. P. Gibson, M. K. Doggett, G. H. Taylor, J. Curtis,  
772 and P. Pasteris, 2008: Physiographically sensitive mapping of climatological temperature  
773 and precipitation across the conterminous United States. *Int. J. Climatol.*, **28**, 2031–2064.
- 774 Delworth, T. and F. Zeng, 2014: Regional rainfall decline in Australia attributed  
775 to anthropogenic greenhouse gases and ozone levels. *Nat. Geosci.*, **7**, 583–587,  
776 doi:10.1038/NGEO2201.
- 777 di Castri, F. and H. Mooney, 1973: *Mediterranean Type Ecosystems: Origin and Structure*.  
778 Ecological Studies 7, Springer Berlin Heidelberg, 405pp.

779 Feitas, A. C. V., J. S. Frederiksen, T. J. O’Kane, and T. Ambrizzi, 2017: Simulated austral  
780 winter response of the Hadley circulation and stationary Rossby wave propagation to a  
781 warming climate. *Clim. Dyn.*, **49**, 521–545.

782 Flocas, H. A., I. Simmonds, J. Kouroutzoglou, K. Keay, M. Hatzaki, V. Bricolas, and D. Asi-  
783 makopoulos, 2010: On cyclonic tracks over the eastern Mediterranean. *J. Climate*, **23**,  
784 5243–5257.

785 Franzke, C. L. E., T. J. O’Kane, D. P. Monselesan, J. S. Risbey, and I. Horenko, 2015:  
786 Systematic attribution of observed Southern Hemisphere circulation trends to external  
787 forcing and internal variability. *Nonlin. Proc. Geophys.*, **22**, 513–525.

788 Gao, Y., L. R. Leung, J. Lu, Y. Liu, M. Huang, and Y. Qian, 2014: Robust spring drying  
789 in the Southwestern US and seasonal migration of wet/dry patterns in a warmer climate.  
790 *Geophys. Res. Lett.*, **41**, 1745–1751, DOI: 10.1002/2014GL059562.

791 Garreaud, R. D. and D. S. Battisti, 1999: Interannual (ENSO) and interdecadal (ENSO-like)  
792 variability in the southern hemisphere tropospheric circulation. *J. Climate*, **12**, 2113–2123.

793 Garreaud, R. D., et al., 2018: The 2010 - 2015 megadrought in central Chile: impacts on  
794 regional hydroclimate and vegetation. *Hydrol. Earth Syst. Sci.*, **21**, 6307–6327.

795 Grise, K. M. and L. M. Polvani, 2011: The response of mid-latitude jets to increased  $CO_2$ :  
796 Distinguishing the roles of sea surface temperature and direct radiative forcing. *Geophys.*  
797 *Res. Lett.*, **41**, 6863–6871, doi:10.1002/2014GL061638.

798 Grise, K. M., et al., 2019: Recent tropical expansion: Natural variability or forced response?  
799 *J. Climate*, doi:10.1175/JCLI-D-18-0444.1, in press.

800 Harris, I., P. D. Jones, T. J. Osborn, and D. H. Lister, 2014: Updated high-resolution grids  
801 of monthly climatic observations - the CRU TS3.10. *Int. J. Climatol.*, **34**, 623–642.

802 Held, I. M. and B. J. Soden, 2006: Robust responses of the hydrological cycle to global  
803 warming. *J. Climate*, **19**, 5686–5699.

804 Hoerling, M. P., J. Eischeid, J. Perlwitz, X. Quan, T. Zhang, and P. Pegion, 2012: On the  
805 increased frequency of Mediterranean drought. *J. Climate*, **25**, 2146–2161.

806 Hoskins, B. and P. J. Valdes, 1990: On the existence of storm tracks. *J. Atmos. Sci.*, **47**,  
807 1854–1864.

808 Hurrell, J. W., 1995: Decadal trends in the North Atlantic Oscillation: Regional tempera-  
809 tures and precipitation. *Science*, **269**, 676–679.

810 Jong, B., M. Ting, and R. Seager, 2016: El Niño’s impact on California precipitation:  
811 seasonality, regionality, and El Niño intensity. *Env. Res. Lett.*, **11**, doi:10.1088/1748–  
812 9326/11/5/054021.

813 Kalnay, E. et al., 1996: The NCEP/NCAR 40-year reanalysis project. *Bull. Am. Meteor.*  
814 *Soc.*, **77**, 437–471.

815 Kelley, C., M. Ting, R. Seager, and Y. Kushnir., 2011: The relative contributions of radiative  
816 forcing and internal climate variability to the late 20th Century winter drying of the  
817 Mediterranean region. *Clim. Dyn.*, **38**, 2001–2015, doi:10.1007/s00382-011-1221-z.

818 Kistler, R., et al., 2001: The NCEP-NCAR 50-year Reanalysis: Monthly means CD-ROM  
819 and documentation. *Bull. Am. Meteor. Soc.*, **82**, 247–268.

820 Lau, K.-M. and K. Kim, 2015: Robust Hadley circulation changes and increasing global  
821 dryness due to  $CO_2$  warming from CMIP5 model projections. *Proc. Nat. Acad. Sci.*, **112**,  
822 3630–3635.

823 Leemans, R. and W. P. Cramer, 1991: The IIASA database for mean monthly values of  
824 temperature, precipitation, and cloudiness on a global terrestrial grid. Tech. rep., IIASA  
825 Technical Report RR-91-018, Laxenburg, Austria.

826 Lionello, P., et al., 2006: Cyclones in the Mediterranean region: Climatology and effects  
827 on the environment. *Mediterranean Climate Variability*, P. Lionello, P. Malanotte-Rizzoli,  
828 and R. Boscolo, Eds., Elsevier, Amsterdam, Netherlands, 325–372.

- 829 Lopez-Parages, J. and B. Rodriguez-Fonseca, 2012: Multidecadal modulation of El  
830 Niño influence on the Euro-Mediterranean rainfall. *Geophys. Res. Lett.*, **39**, L02704  
831 doi:10.1029/2011GL050049.
- 832 Lopez-Parages, J., B. Rodriguez-Fonseca, D. Dommenges, and C. Frauen, 2016: ENSO influ-  
833 ences on the North Atlantic-European climate: a non-linear and non-stationary approach.  
834 *Clim. Dyn.*, **47**, 2071–2084, doi:10.1007/s00382-015-2951-0.
- 835 Lorenz, D. J. and E. T. DeWeaver, 2007: The response of the extratropical hydrological  
836 cycle to global warming. *J. Climate*, **20**, 3470–3484.
- 837 Lu, J., G. Vecchi, and T. Reichler, 2007: Expansion of the Hadley Cell under global warming.  
838 *Geophys. Res. Lett.*, **34**, doi:10.1029/2006GL028443.
- 839 Meneghini, B., I. Simmonds, and I. N. Smith, 2007: Association between Australian rainfall  
840 and the Southern Annular Mode. *Int. J. Climatol.*, **27**, 109–121, doi:10.1002/joc.1370.
- 841 O’Gorman, P. and C. J. Muller, 2010: How closely do changes in surface and column water  
842 vapor follow Clausius-Clapeyron scaling in climate change simulations? *Env. Res. Lett.*,  
843 **5**, doi:10.1088/1748-9326/5/2/0252077.
- 844 O’Kane, T. J., D. P. Monselesan, and J. S. Risbey, 2017: A multiscale examination of the  
845 Pacific-South America pattern. *Mon. Wea. Rev.*, **145**, 379–402.
- 846 Philippon, N., M. Rouault, Y. Richard, and A. Favre, 1985: The influence of ENSO on  
847 winter rainfall in South Africa. *Int. J. Climatol.*, **32**, 2333–2347.
- 848 Polade, S. D., A. Gershunov, D. R. Cayan, M. D. Dettinger, and D. W. Pierce, 2017: Precip-  
849 itation in a warming world: Assessing projected hydro-climate changes in California and  
850 other Mediterranean climate regions. *Scientific Reports*, **7**, 10783, doi:10.1038/s41598-  
851 017-11285-y.
- 852 Polvani, L. M., D. W. Waugh, G. J. P. Correa, and S. Son, 2011: Stratospheric ozone  
853 depletion: The main driver of 20th century atmospheric circulation changes in the southern  
854 hemisphere. *J. Climate*, **24**, 795–812, doi: 10.1175/2010JCLI3772.1.



- 855 Pozo-Vasquez, D., M. J. Esteban-Parra, F. S. Rodrigo, and Y. Castro-Diez, 2001: The  
856 association between ENSO and winter atmospheric circulation and temperature in the  
857 North Atlantic region. *J. Climate*, **14**, 3408–3420.
- 858 Pozo-Vasquez, D., S. R. Gamis-Fortis, J. Tovar-Pescador, M. J. Esteban-Parra, and  
859 Y. Castro-Diez, 2005: El Niño-Southern Oscillation events and associated European winter  
860 precipitation anomalies. *Int. J. Climatol.*, **25**, 17–31.
- 861 Rayner, N., D. Parker, E. Horton, C. Folland, L. Alexander, D. Rowell, E. Kent, and  
862 A. Kaplan, 2003: Global analyses of sea surface temperature, sea ice, and night ma-  
863 rine air temperature since the late nineteenth century. *J. Geophys. Res.*, **108**, 4407,  
864 10.1029/2002JD002670.
- 865 Reason, C., M. Rouault, J.-L. Melice, and D. Jagadheesha, 2002: Interannual winter rainfall  
866 variability in SW South Africa and large scale ocean-atmosphere interactions. *Meteor.*  
867 *Atm. Phys.*, **80**, 19–29.
- 868 Risbey, J. S., M. J. Pook, P. C. McIntosh, M. C. Wheeler, and H. H. Hendon, 2009: On the  
869 remote drivers of rainfall variability in Australia. *J. Climate*, **137**, 3233–3253.
- 870 Rodwell, M. J. and B. J. Hoskins, 1996: Monsoons and the dynamics of deserts. *Quart. J.*  
871 *Roy. Meteor. Soc.*, **122**, 1385–1404.
- 872 Rodwell, M. J. and B. J. Hoskins, 2001: Subtropical anticyclones and summer monsoons. *J.*  
873 *Climate*, **14**, 3192–3211.
- 874 Rowell, D. P., 2013: Simulating SST teleconnections to Africa: What is the state of the art?  
875 *J. Climate*, **26**, 5397–5418.
- 876 Rubel, F. and M. Kottek, 2010: Observed and projected climate shifts 1901-2100 depicted  
877 by world maps of the Koppen-Geiger climate classification. *Meteorol. Z.*, **7**, 135–141.
- 878 Scaife, A., et al., 2014: Skillful long-range predictions of European and North American  
879 winters. *Geophys. Res. Lett.*, **41**, doi10.1029/2014GL059637.

- 880 Schneider, T., 2006: The general circulation of the atmosphere. *Ann. Rev. Earth Planet Sci.*,  
881 **34**, 655–688.
- 882 Schneider, T., T. Bischoff, and H. Plotka, 2015: Physics of change in synoptic midlatitude  
883 temperature variability. *J. Climate*, **28**, 2312–2331.
- 884 Schneider, U., A. Becker, P. Finger, A. Meyer-Christoffer, B. Rudolf, and M. Ziese, 2011:  
885 GPCC full data reanalysis version 6.0 at 0.5°: monthly land surface precipitation from rain  
886 gauges built on GTS-based and historic data. Tech. rep., Global Precipitation Climatology  
887 Centre, doi:10.5676/DWD\_GPCC/FD\_M\_V6\_050.
- 888 Seager, R., N. Harnik, Y. Kushnir, W. Robinson, and J. Miller, 2003a: Mechanisms of  
889 hemispherically symmetric climate variability. *J. Climate*, **16**, 2960–2978.
- 890 Seager, R. and N. Henderson, 2013: Diagnostic computation of moisture budgets in the  
891 ERA-Interim Reanalysis with reference to analysis of CMIP-archived atmospheric model  
892 data. *J. Climate*, **26**, 7876–7901.
- 893 Seager, R., M. Hoerling, S. Schubert, H. Wang, B. Lyon, A. Kumar, J. Nakamura, and  
894 N. Henderson, 2014a: Causes and predictability of the 2011-14 California drought. Tech.  
895 rep., National Oceanic and Atmospheric Administration, DTF/NIDIS Assessment Report,  
896 doi:10.7289/V58K771F, 42 pp.
- 897 Seager, R., M. Hoerling, S. Schubert, H. Wang, B. Lyon, A. Kumar, J. Nakamura, and  
898 N. Henderson, 2015: Causes of the 2011-14 California drought. *J. Climate*, **28**, 6997–7024.
- 899 Seager, R., H. Liu, N. Henderson, I. Simpson, C. Kelley, T. Shaw, Y. Kushnir, and M. Ting,  
900 2014b: Causes of increasing aridification of the Mediterranean region in response to rising  
901 greenhouse gases. *J. Climate*, **27**, 4655–4676.
- 902 Seager, R., R. Murtugudde, N. Naik, A. Clement, N. Gordon, and J. Miller, 2003b: Air-  
903 sea interaction and the seasonal cycle of the subtropical anticyclones. *J. Climate*, **16**,  
904 1948–1966.

905 Seager, R., N. Naik, and G. A. Vecchi, 2010: Thermodynamic and dynamic mechanisms for  
906 large-scale changes in the hydrological cycle in response to global warming. *J. Climate*,  
907 **23**, 4651–4668.

908 Seager, R., D. Neelin, I. Simpson, H. Liu, N. Henderson, T. Shaw, Y. Kushnir, and M. Ting,  
909 2014c: Dynamical and thermodynamical causes of large-scale changes in the hydrological  
910 cycle over North America in response to global warming. *J. Climate*, **27**, 7921–7948.

911 Sherwood, S. C., W. Ingram, Y. Tsushima, M. Satoh, M. Roberts, P. Liugi Vidale, and P. A.  
912 O’Gorman, 2010: Relative humidity changes in a warmer climate. *J. Geophys. Res.*, **115**,  
913 D09104,doi:10.1029/2009JD012585.

914 Simpkins, G., 2018: Running dry. *Nature Clim. Ch.*, **8**, 369.

915 Simpson, I., R. Seager, T. Shaw, and M. Ting, 2015: Mediterranean summer climate and  
916 the importance of Middle East topography. *J. Climate*, **28**, 1977–1996.

917 Simpson, I., R. Seager, M. Ting, and T. A. Shaw, 2016: Causes of change in northern  
918 hemisphere winter meridional wind and regional hydroclimate. *Nature. Clim. Ch.*, **6**, 65–  
919 70,doi:10.1038/NCLIMATE2783.

920 Simpson, I., T. Shaw, and R. Seager, 2014: A diagnosis of the seasonally and longitudinally  
921 varying mid-latitude circulation response to global warming. *J. Atmos. Sci.*, **71**, 2489–  
922 2515.

923 Smith, I. N., P. McIntosh, T. J. Ansell, C. J. C. Reason, and K. McInnes, 2000: Southwest  
924 western Australian winter rainfall and its association with Indian Ocean climate variability.  
925 *Int. J. Climatol.*, **20**, 1913–1930.

926 Taylor, K. E., R. J. Stouffer, and G. A. Meehl, 2012: An overview of CMIP5 and the  
927 experiment design. *Bulletin of the American Meteorological Society*, **93**, 485–498.

928 Thompson, D. W. J., S. Solomon, P. J. Kushner, M. H. England, K. M. Grise, and D. J.  
929 Karoly, 2011: Signatures of the Antarctic ozone hole in southern hemisphere surface cli-  
930 mate change. *Nat. Geo.*, **4**, 741–749.

- 931 Thompson, D. W. J. and J. M. Wallace, 2000: Annular modes in the extratropical circulation:  
932 Part I: Month-to-month variability. *J. Climate*, **13**, 1000–1016.
- 933 Ting, M., R. Seager, C. Li, H. Liu, and N. Henderson, 2018: Mechanisms of future spring  
934 drying in the southwestern United States in CMIP5 models. *J. Climate*, **31**, 4265–4279.
- 935 Trenberth, K., 1991: Storm tracks in the Southern Hemisphere. *J. Atmos. Sci.*, **48**, 2159–  
936 2178.
- 937 Trenberth, K., G. W. Branstator, D. Karoly, A. Kumar, N. Lau, and C. Ropelewski, 1998:  
938 Progress during TOGA in understanding and modeling global teleconnections associated  
939 with tropical sea surface temperature. *J. Geophys. Res.*, **103**, 14 291–14 324.
- 940 Trenberth, K., J. T. Fasullo, and J. Mackaro, 2011: Atmospheric moisture transport from  
941 ocean to land and global energy flows in Reanalyses. *J. Climate*, **24**, 4907–4924.
- 942 Trigo, I. F., T. D. Davies, and G. R. Bigg, 1999: Objective climatology of cyclones in the  
943 Mediterranean region. *J. Climate*, **12**, 1685–1696.
- 944 Williams, A. P., et al., 2015: Correlations between components of the water balance and  
945 burned area reveal new insights for predicting forest-fire area in the southwest United  
946 States. *Int. J. Wildland Fire*, **24**, 14–26.
- 947 Wolski, P., 2018: How severe is Cape Town’s “Day Zero” drought? *Significance*, **15.2**, 24–27.
- 948 Woollings, T. and M. Blackburn, 2012: The North Atlantic jet stream under climate change  
949 and its relation to the NAO and EA patterns. *J. Climate*, **25**, 886–902.
- 950 Wright, J. S., A. S. Sobel, and J. Galewsky, 2010: Diagnosis of zonal mean relative humidity  
951 changes in a warmer climate. *J. Climate*, **23**, 4556–4569.
- 952 Yin, J. H., 2005: A consistent poleward shift of the storm tracks in simulations of 21st  
953 century climate. *Geophys. Res. Lett.*, **32**, L18 701, doi:10/1029/2005GL023 684.
- 954 Zappa, G., B. J. Hoskins, and T. G. Shepherd, 2015: The dependence of wintertime Mediter-  
955 ranean precipitation on the atmospheric circulation response to climate change. *Env. Res.*  
956 *Lett.*, **10**, doi:10.1088/1748–9326/10/12/129 501.

957 **List of Tables**

958 1 CMIP5 models used in this study with information on host institute, resolu-  
959 tions (L refers to number of vertical levels, T to triangular truncation and C  
960 to cubed sphere) and ensemble sizes. 37

Institute	Model	Resolution (lon x lat), level	Ensemble size	
			20thC	rcp85
Beijing Climate Center (BCC)	1. bcc-csm1-1	T42, L26	1	1
	2. bcc-csm1-1-m	T106, L26	1	1
College of Global Change and Earth System Science, Beijing Normal University (BNU)	3. BNU-ESM	T42, L26	1	1
Canadian Centre for Climate Modeling and Analysis (CC-Cma)	4. CanESM2	T63 (1.875°x1.875°), L35	1	1
National Center for Atmospheric Research (NCAR)	5. CCSM4	288x200 (1.25°x0.9°), L26	1	1
Centro Euro-Mediterraneo per I Cambiamenti Climatici (CMCC)	6. CMCC-CM	T159, L31	1	1
Centre National de Recherches Meteorologiques / Centre European de Recherche et Formation Avancees en Calcul Scientifique (CNRM-CERFACS)	7. CNRM-CM5	T127(1.4°x1.4°), L31	1	1
Commonwealth Scientific and Industrial Research Organisation in collaboration with the Queensland Climate Change Centre of Excellence (CSIRO-QCCCE)	8. CSIRO-Mk3-6-0	T63(1.875°x1.875°), L18	1	1
Institute of Atmospheric Physics, Chinese Academy of Sciences and Tsinghua University (LASG-CESS)	9. FGOALS-g2	128x60, L26	2	1
Geophysical Fluid Dynamics Laboratory (NOAA GFDL)	10. GFDL-CM3	C48 (2.5°x2.0°), L48	5	1
	11. GFDL-ESM2G	144x90 (2.5°x2.0°), L24	1	1
	12. GFDL-ESM2M	144x90 (2.5°x2.0°), L24	1	1
NASA Goddard Institute for Space Studies (NASA GISS)	13. GISS-E2-H	2.5°x2°, L40	1	1
	14. GISS-E2-R	2.5°x2°, L40	1	1
Institut Pierre-Simon Laplace (IPSL)	15. IPSL-CM5A-LR	3.75°x1.875°, L39	6	3
	16. IPSL-CM5A-MR	2.5°x1.25°, L39	2	1
	17. IPSL-CM5B-LR	96x96 (3.75°x1.875°), L39	1	1
Atmosphere and Ocean Research Institute (The University of Tokyo), National Institute for Environmental Studies, and Japan Agency for Marine-Earth Science and Technology (AORI/NIES/JAMSTEC)	18. MIROC5	T85, L40	5	1
	19. MIROC-ESM	T42, L80	3	1
	20. MIROC-ESM-CHEM	T42, L80	1	1
Meteorological Research Institute (MRI)	21. MRI-CGCM3	TL159 (1.125°x1.125°), L48	1	1
Norwegian Climate Centre (NCC)	22. NorESM1-M	144x96 (2.5°x1.875°), L26	3	1

TABLE 1. CMIP5 models used in this study with information on host institute, resolutions (L refers to number of vertical levels, T to triangular truncation and C to cubed sphere) and ensemble sizes.

## 961 List of Figures

- 962 1 Location of Mediterranean-type climate regions (color). Burgundy color shows  
963 the hot summer type of Mediterranean climate (Csa in the Koppen classifica-  
964 tion) and orange shows the warm summer type of Mediterranean climate (Csb  
965 in the Koppen classification). Also shown as contours is the annual mean pre-  
966 cipitation over land from CRU TS v3.25 in mm/month, with dotted contours  
967 indicating values less than 50mm/month. Area averages are taken over the  
968 Mediterranean climate areas shown by the colored areas within the red boxes. 42
- 969 2 Precipitation over land (mm/month) for northern hemisphere winter/southern  
970 hemisphere summer (top) and northern hemisphere summer/southern hemi-  
971 sphere winter (bottom). Also shown are sub-monthly 200hPa meridional ve-  
972 locity variance ( $m^2/s^{-2}$ ), a measure of the mid-latitude storm track (left) and  
973 sea level pressure (hPa, right). 43
- 974 3 The climatological seasonal cycles and variability of precipitation (left) and  
975 temperature (right) in the Mediterranean climate regions. The means are  
976 shown by the lines and the box and whiskers plotted for each month show  
977 the median (line across box), 25th and 75th percentiles (edges of box), range  
978 and outliers (beyond  $2.7 \sigma$  for a normal distribution) as red crosses. Units are  
979 mm/month and deg C. 44
- 980 4 The regression of SST (colors, deg C) and 200hPa geopotential heights (con-  
981 tours, m) onto the winter precipitation time series of each Mediterranean-type  
982 climate region, after detrending. The SSTs are plotted only where the relation  
983 is statistically significant at the 5% level. 45

- 984 5 The time histories of winter precipitation (left) and temperature (right) in  
985 the Mediterranean-type climate regions for observations (black line) and the  
986 SST-forced CAM5.3 model ensemble mean precipitation (green, left) and tem-  
987 perature (red, right) together with ensemble spread (shading). At bottom left  
988 the numbers are the correlation coefficient between the observations and the  
989 ensemble mean and, for temperature the values in parentheses are for linearly  
990 detrended data, and bold values are significant at the 5% level according to a  
991 two-sided t-test. Units are mm/month and deg C. 46
- 992 6 As in Figure 4 but for the ensemble mean of the SST-forced simulations with  
993 the CAM5.3 model isolating the ocean-driven component of modeled winter  
994 precipitation variability in the Mediterranean-type climate regions. 47
- 995 7 The linear trend over 1901 to 2016 of winter precipitation showing the Mediter-  
996 ranean climate regions. Stippled locations mark significance of the trend at  
997 the 5% level according to a two-sided t-test. Units are mm/month change  
998 over the 116 years. 48
- 999 8 Upper panel: same as Figure 7 but for the multimodel mean of the CMIP5  
1000 models using the historical simulation for 1901 to 2005 and the RCP85 emis-  
1001 sions scenario for 2006 to 2016. Stippled locations mark where three quarters  
1002 of the models agree on sign of change and with sign of change of the ensemble  
1003 mean. In the lower panel the distribution of modeled trends are shown by box  
1004 and whisker plots: the median, 25th and 75th percentiles are shown by the  
1005 horizontal line across the box and its limits, the range by whiskers, outliers by  
1006 a red cross and the mean by a black asterisk. Also shown are the CRU, GPCC  
1007 and, for California and the Pacific northwest, the PRISM trends. Units are  
1008 mm/month change over 116 years. 49



1009	9	The number of models (out of 22) that agree on the sign of change of winter precipitation and also agree with the sign of change of the model ensemble mean. Green colors indicate agreement is for wetting and brown colors for drying. Stippling marks where three quarters or more of models agree.	50
1010			
1011			
1012			
1013	10	CMIP5 multimodel mean-projected changes in the winter moisture budget in the North America region for the near term future (2021-2040) minus the recent past (1979-2005) using emissions scenario RCP85 and the historical simulations. Shown are change in a) $P$ , b) $E$ , c) $P - E$ , d) the mean flow moisture convergence, e) the component of d) related to mass divergence, f) the component of d) related to moisture advection, g) the surface term and h) the transient eddy moisture convergence. Units are mm/day.	51
1014			
1015			
1016			
1017			
1018			
1019			
1020	11	Same as Figure 10 but for the Mediterranean region.	52
1021	12	Same as Figure 10 but for the South America region.	53
1022	13	Same as Figure 10 but for the Africa and Australia region.	54
1023	14	Further breakdown of the CMIP5 multimodel mean-projected changes in the winter moisture budget here for the South America region. Changes in the mean flow moisture convergence are broken down into components due to circulation changes (dynamic component, left) and moisture changes (thermodynamic component, right) and related to mass divergence (upper) and moisture advection (lower). Units are mm/day.	55
1024			
1025			
1026			
1027			
1028			
1029	15	Same as Figure 14 but for the Africa and Australia region.	56
1030	16	The climatological specific humidity integrated from surface to 600hPa (color) and 850hPa winds (vectors) (top) and the 2021-2040 minus 1979-2005 change in these (bottom) for the southern hemisphere. Units are $kg/m^2$ and $m/s$ .	57
1031			
1032			

1033 17 Figure A1. The CRU TS3.25 observed (top) and CMIP5 multimodel mean  
1034 (bottom) difference in winter precipitation for 1997-2016 minus 1971-1990.  
1035 In the upper panel for the observed data the tick marks show where the  
1036 differences between the means of the two-decade periods is significant at the  
1037 10% level according to a two-sided t-test. In the lower panel for the models  
1038 the tick marks show where 3/4 of the models agree on the sign of the change  
1039 and agree with the sign of the multimodel mean change. Units are *mm/day*. 58

Temperate Dry Summer (Cs), Hot Summer (a-burgundy) Warm Summer (b-orange)  
 CRU Mean Annual Precip (contours)

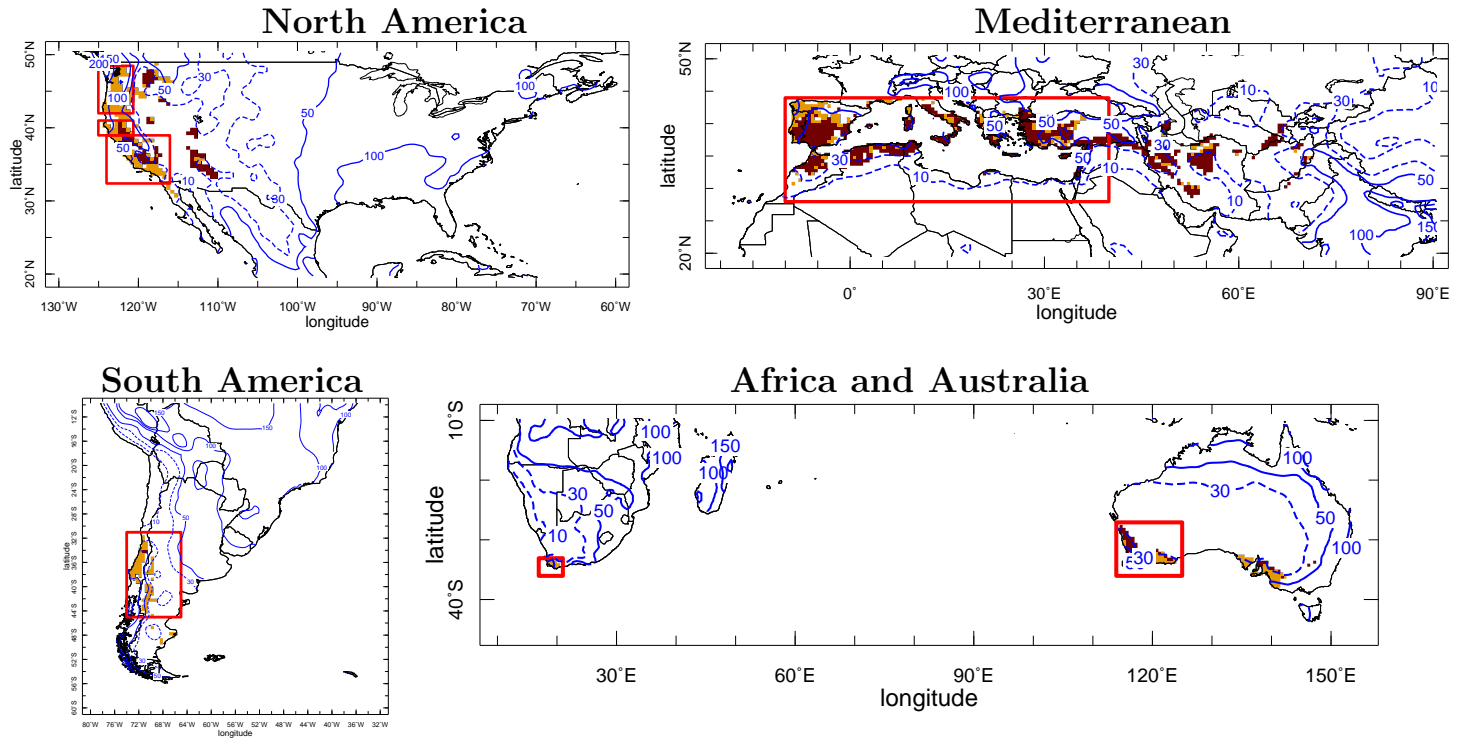


FIG. 1. Location of Mediterranean-type climate regions (color). Burgundy color shows the hot summer type of Mediterranean climate (Csa in the Koppen classification) and orange shows the warm summer type of Mediterranean climate (Csb in the Koppen classification). Also shown as contours is the annual mean precipitation over land from CRU TS v3.25 in mm/month, with dotted contours indicating values less than 50mm/month. Area averages are taken over the Mediterranean climate areas shown by the colored areas within the red boxes.

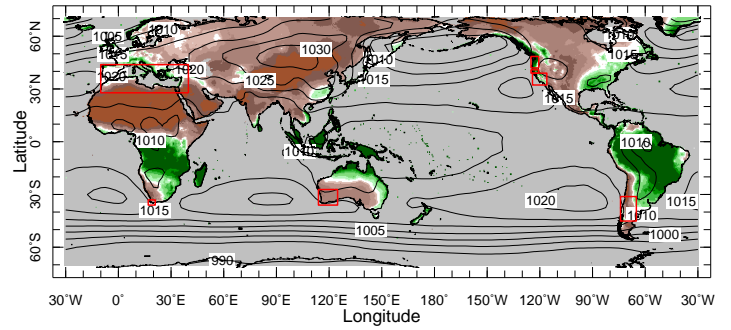
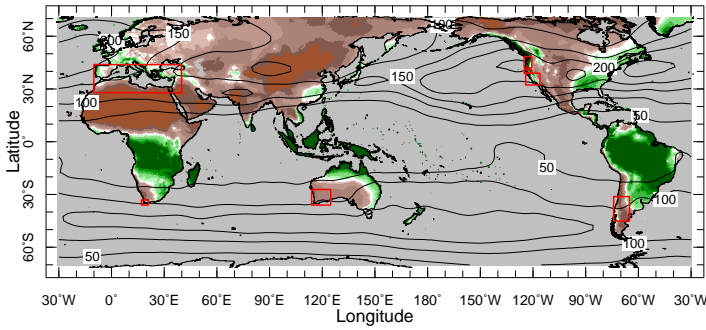
# Seasonal Observed Climatology

Precipitation (color)

200 mb  $V'^2$  (contours)

SLP (contours)

NH Winter, SH Summer



NH Summer, SH Winter

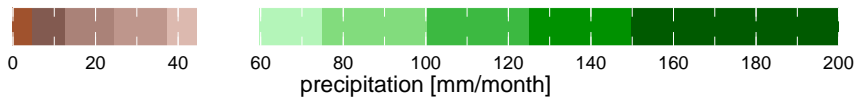
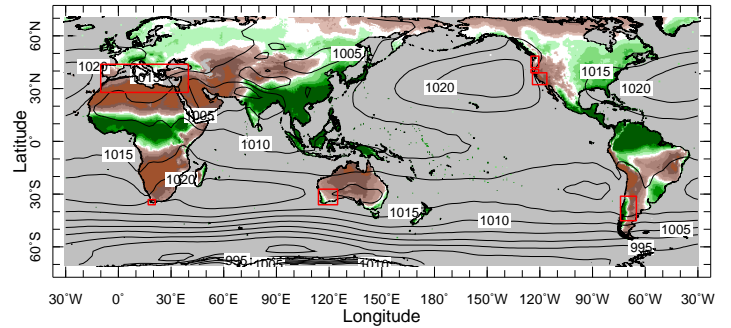
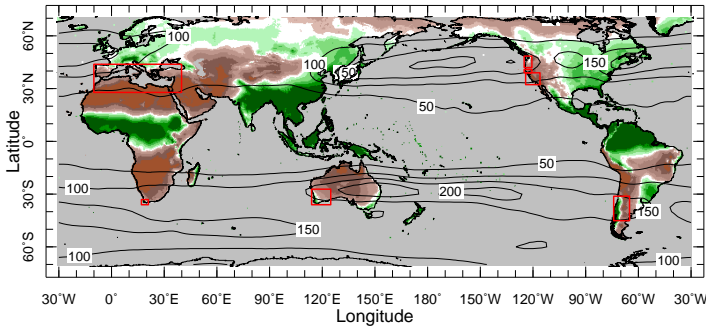


FIG. 2. Precipitation over land (mm/month) for northern hemisphere winter/southern hemisphere summer (top) and northern hemisphere summer/southern hemisphere winter (bottom). Also shown are sub-monthly 200hPa meridional velocity variance ( $m^2/s^2$ ), a measure of the mid-latitude storm track (left) and sea level pressure (hPa, right).

## Csa and Csb, Precip (green), Temp (orange)

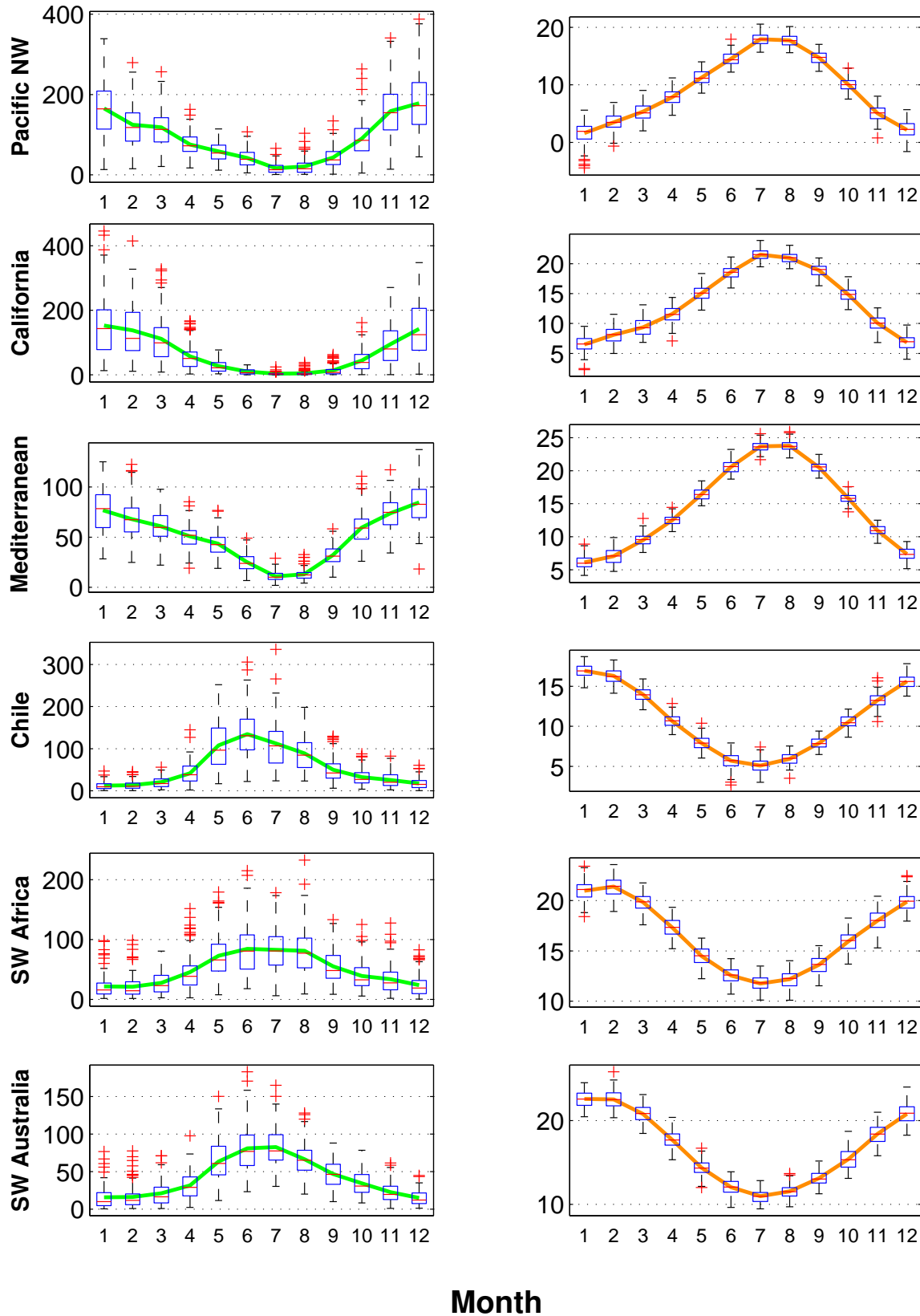


FIG. 3. The climatological seasonal cycles and variability of precipitation (left) and temperature (right) in the Mediterranean climate regions. The means are shown by the lines and the box and whiskers plotted for each month show the median (line across box), 25th and 75th percentiles (edges of box), range and outliers (beyond  $2.7 \sigma$  for a normal distribution) as red crosses. Units are mm/month and deg C.

# Detrended NCEP Winter Sig SST (color), 200 hPa $\phi$ (contours)

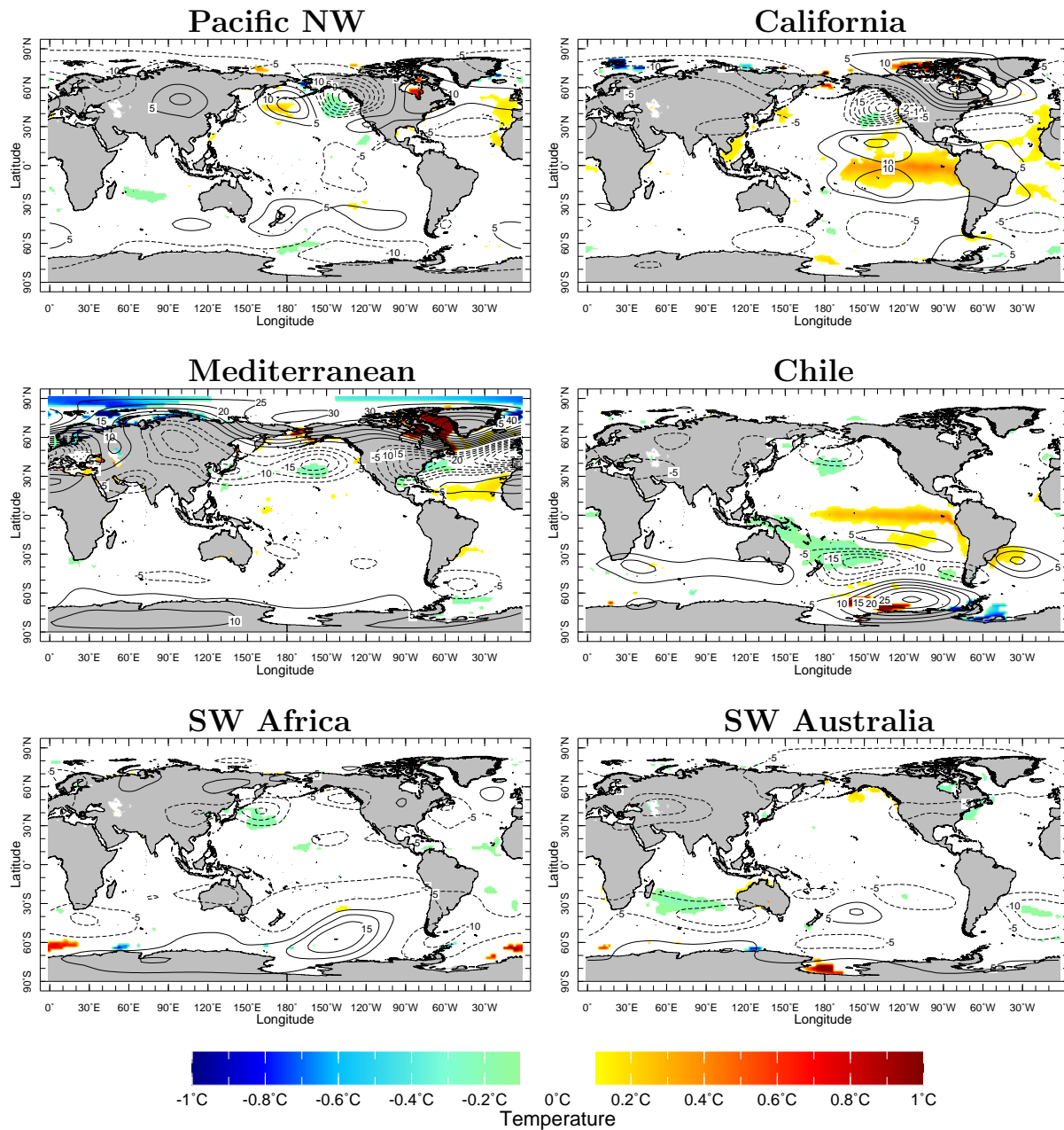


FIG. 4. The regression of SST (colors, deg C) and 200hPa geopotential heights (contours, m) onto the winter precipitation time series of each Mediterranean-type climate region, after detrending. The SSTs are plotted only where the relation is statistically significant at the 5% level.

CAM5 GOGA Winter Csa and Csb, Precip (green), Temp (orange), Min to Max (shade), Obs (black)

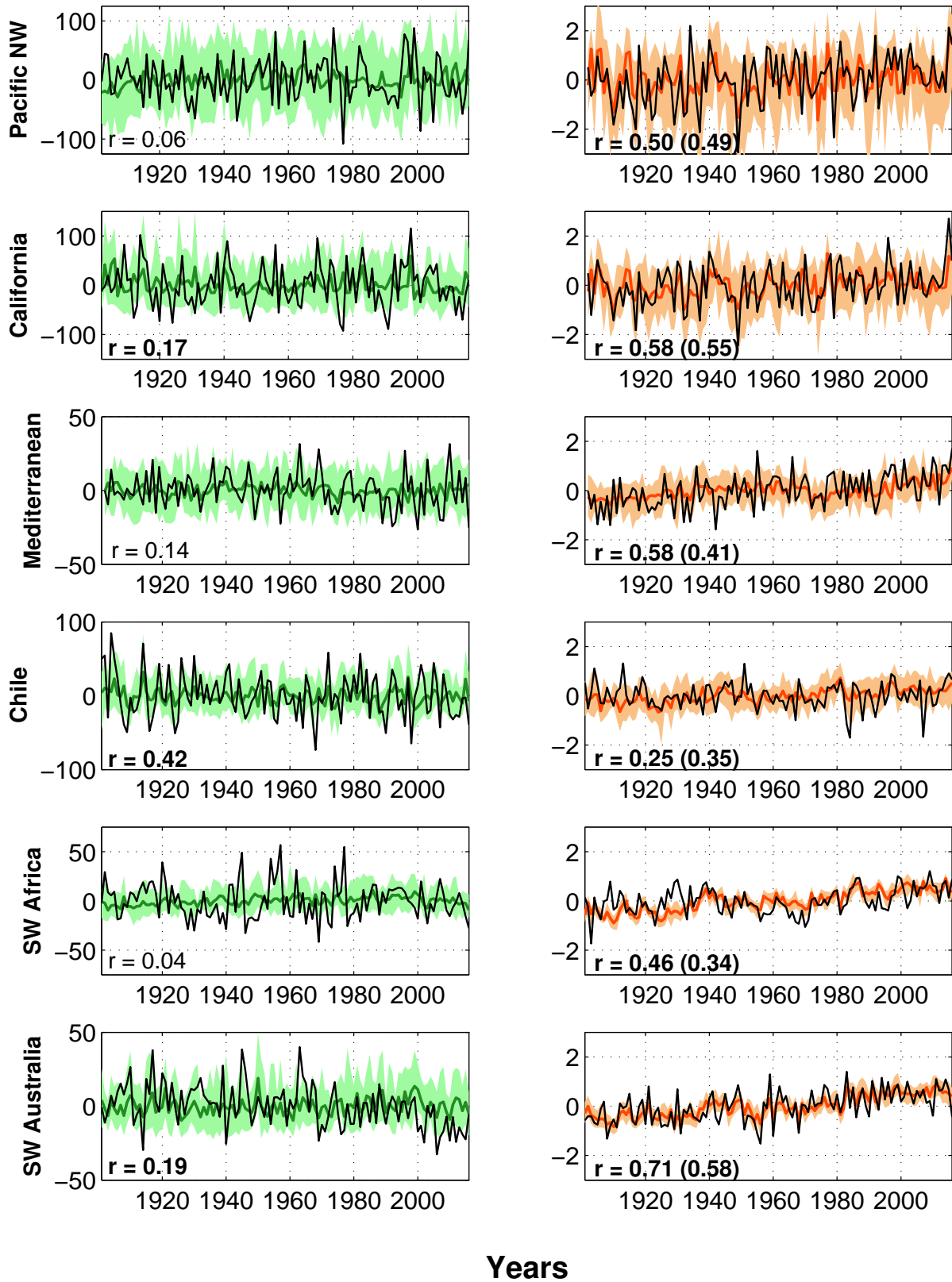


FIG. 5. The time histories of winter precipitation (left) and temperature (right) in the Mediterranean-type climate regions for observations (black line) and the SST-forced CAM5.3 model ensemble mean precipitation (green, left) and temperature (red, right) together with ensemble spread (shading). At bottom left the numbers are the correlation coefficient between the observations and the ensemble mean and, for temperature the values in parentheses are for linearly detrended data, and bold values are significant at the 5% level according to a two-sided t-test. Units are mm/month and deg C.

Detrend CAM5 1949-2016 Winter Precip Regr Sig SST (color), 200 hPa  $\phi$  (contours)

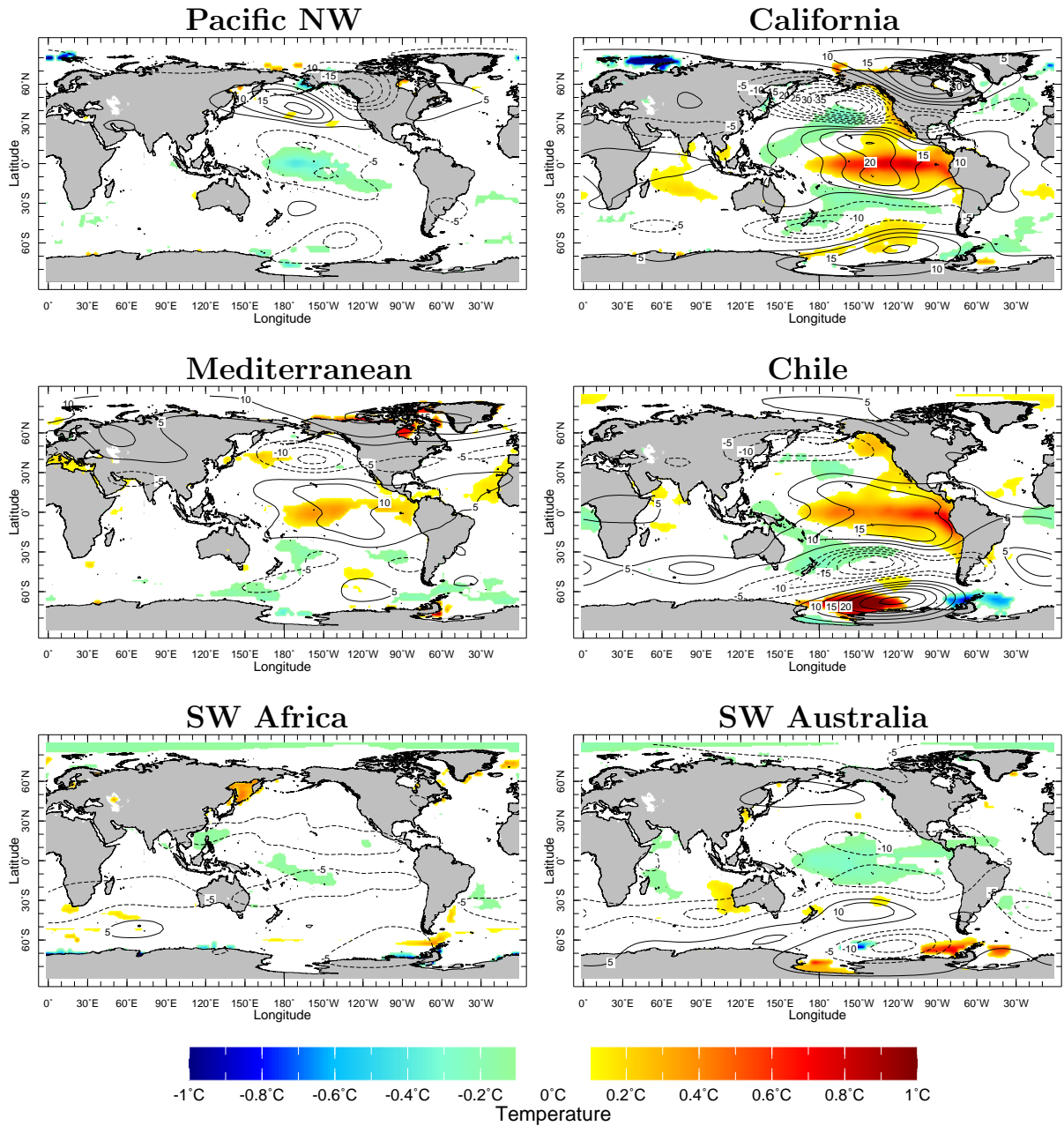


FIG. 6. As in Figure 4 but for the ensemble mean of the SST-forced simulations with the CAM5.3 model isolating the ocean-driven component of modeled winter precipitation variability in the Mediterranean-type climate regions.



## CRU TS3.25 Winter Precipitation Trend 1901-2016

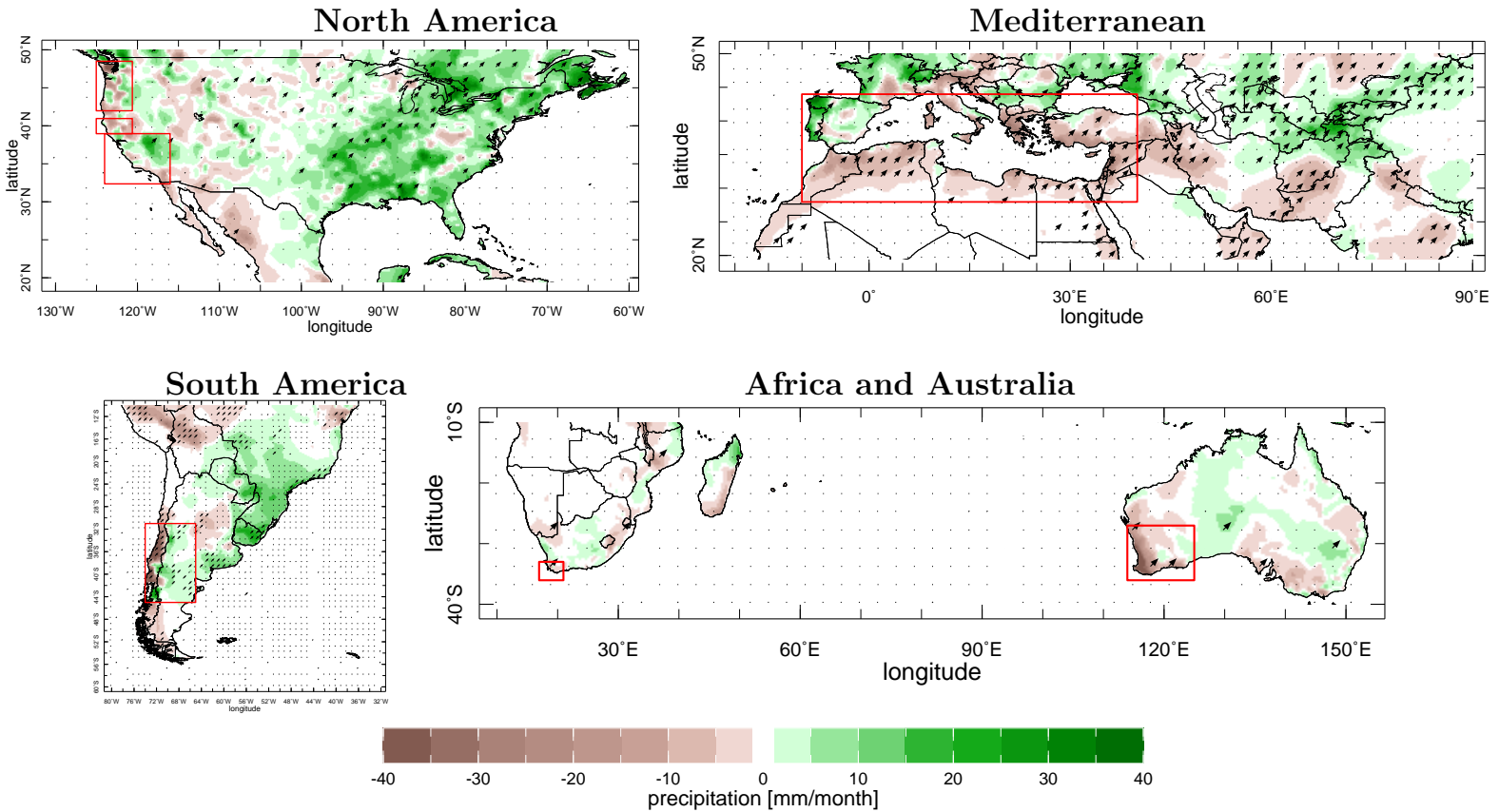
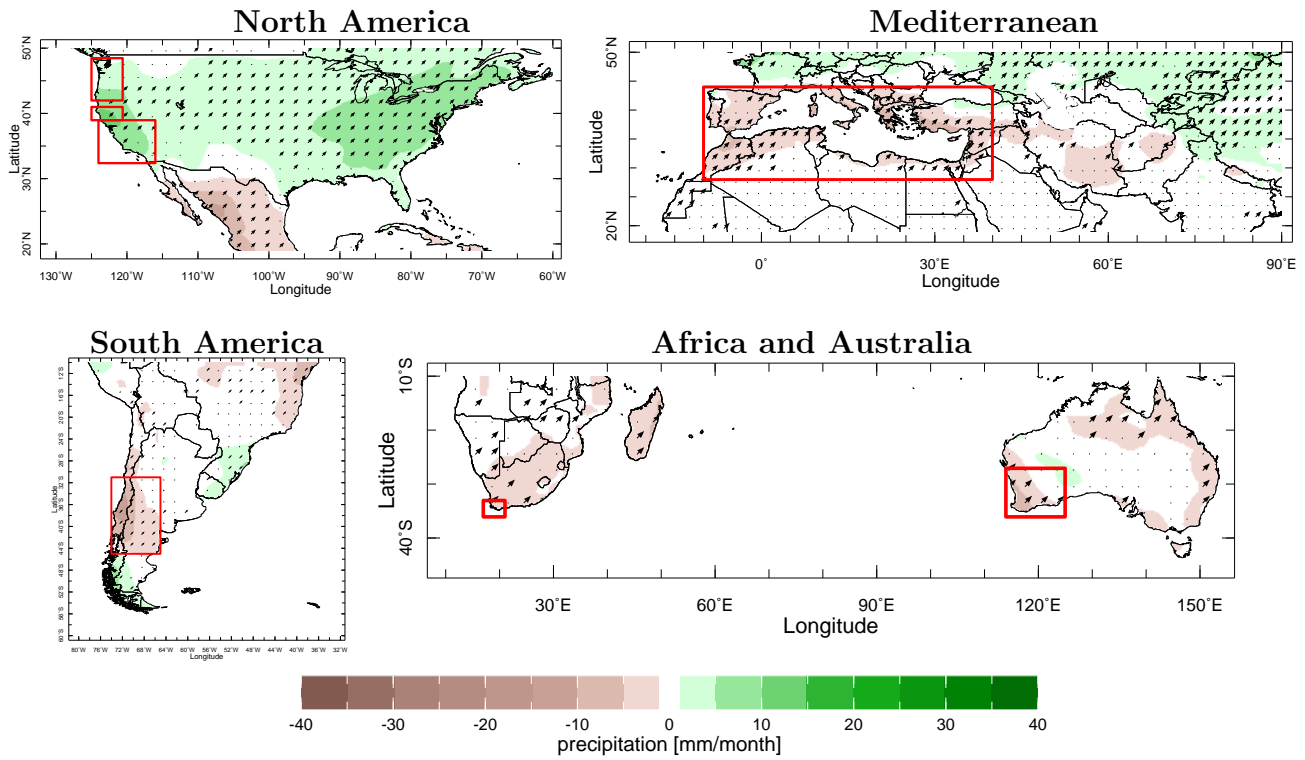


FIG. 7. The linear trend over 1901 to 2016 of winter precipitation showing the Mediterranean climate regions. Stippled locations mark significance of the trend at the 5% level according to a two-sided t-test. Units are mm/month change over the 116 years.

CMIP5 Winter Precipitation Trend (color) Hatch (sigificant) 1901-2016



CMIP5 Winter Csa and Csb Precip Trend, Mean (\*), CRU (x), GPCC (o), PRISM (v)

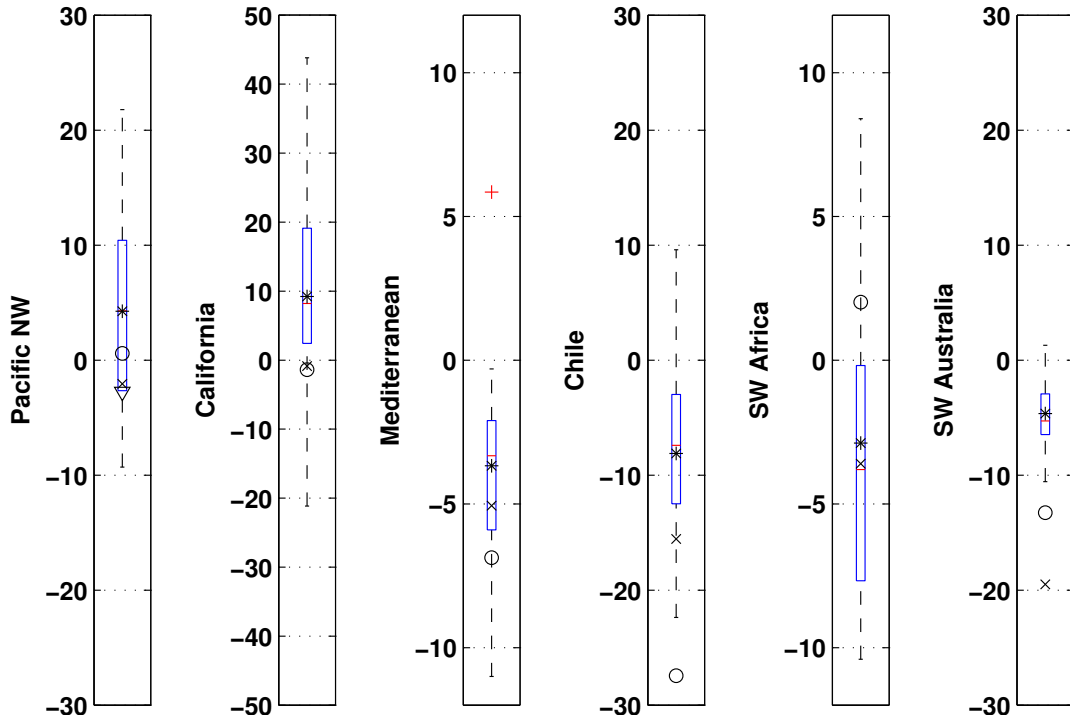


FIG. 8. Upper panel: same as Figure 7 but for the multimodel mean of the CMIP5 models using the historical simulation for 1901 to 2005 and the RCP85 emissions scenario for 2006 to 2016. Stippled locations mark where three quarters of the models agree on sign of change and with sign of change of the ensemble mean. In the lower panel the distribution of modeled trends are shown by box and whisker plots: the median, 25th and 75th percentiles are shown by the horizontal line across the box and its limits, the range by whiskers, outliers by a red cross and the mean by a black asterisk. Also shown are the CRU, GPCC and, for California and the Pacific northwest, the PRISM trends. Units are mm/month change over 116 years.

CMIP5, multi model mean  $\overline{\overline{P}}$ , (2021-2040) - (1979-2005), Significant (dots)

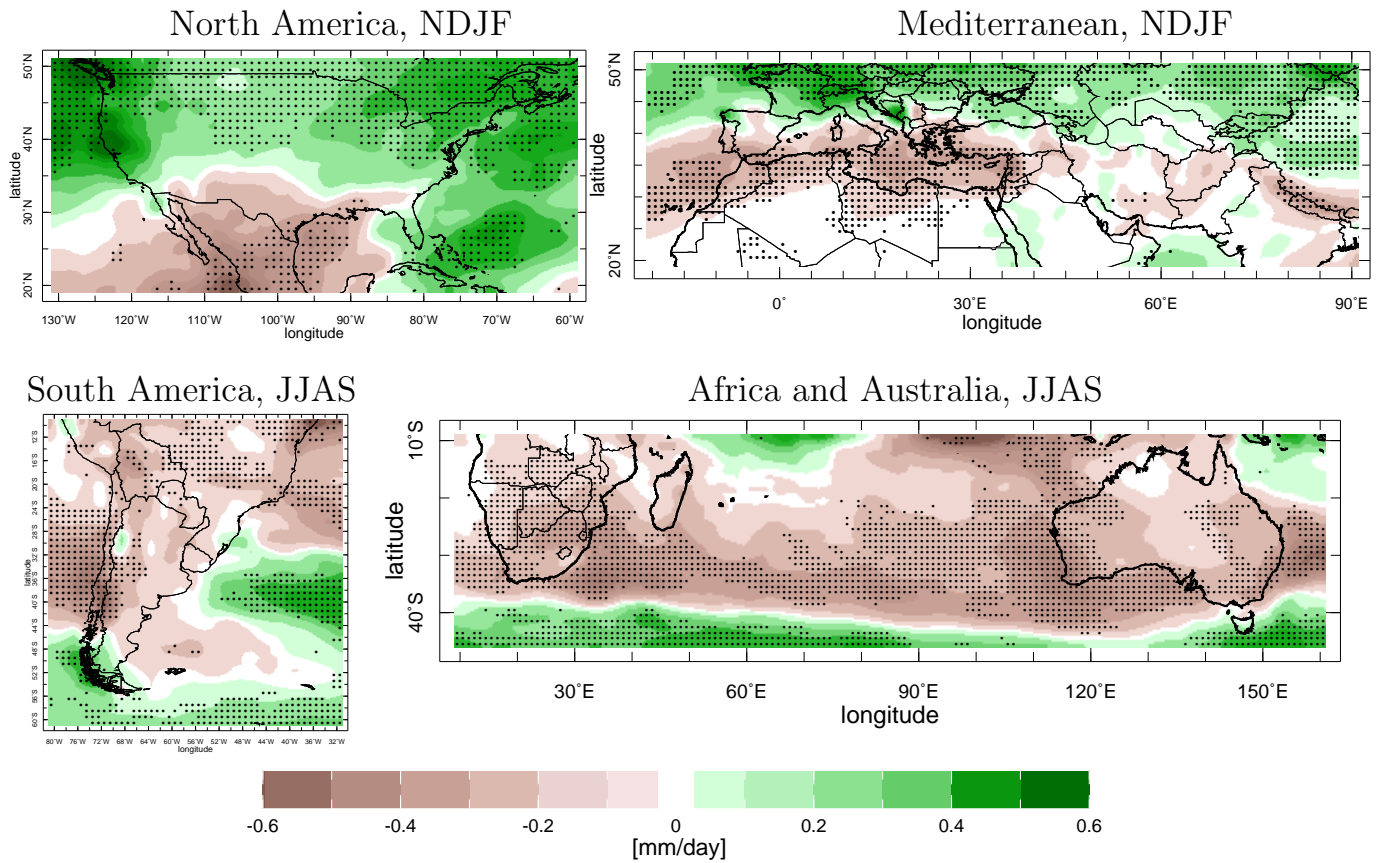


FIG. 9. The number of models (out of 22) that agree on the sign of change of winter precipitation and also agree with the sign of change of the model ensemble mean. Green colors indicate agreement is for wetting and brown colors for drying. Stippling marks where three quarters or more of models agree.





CMIP5, South America, (2021-2040) - (1979-2005), JJAS

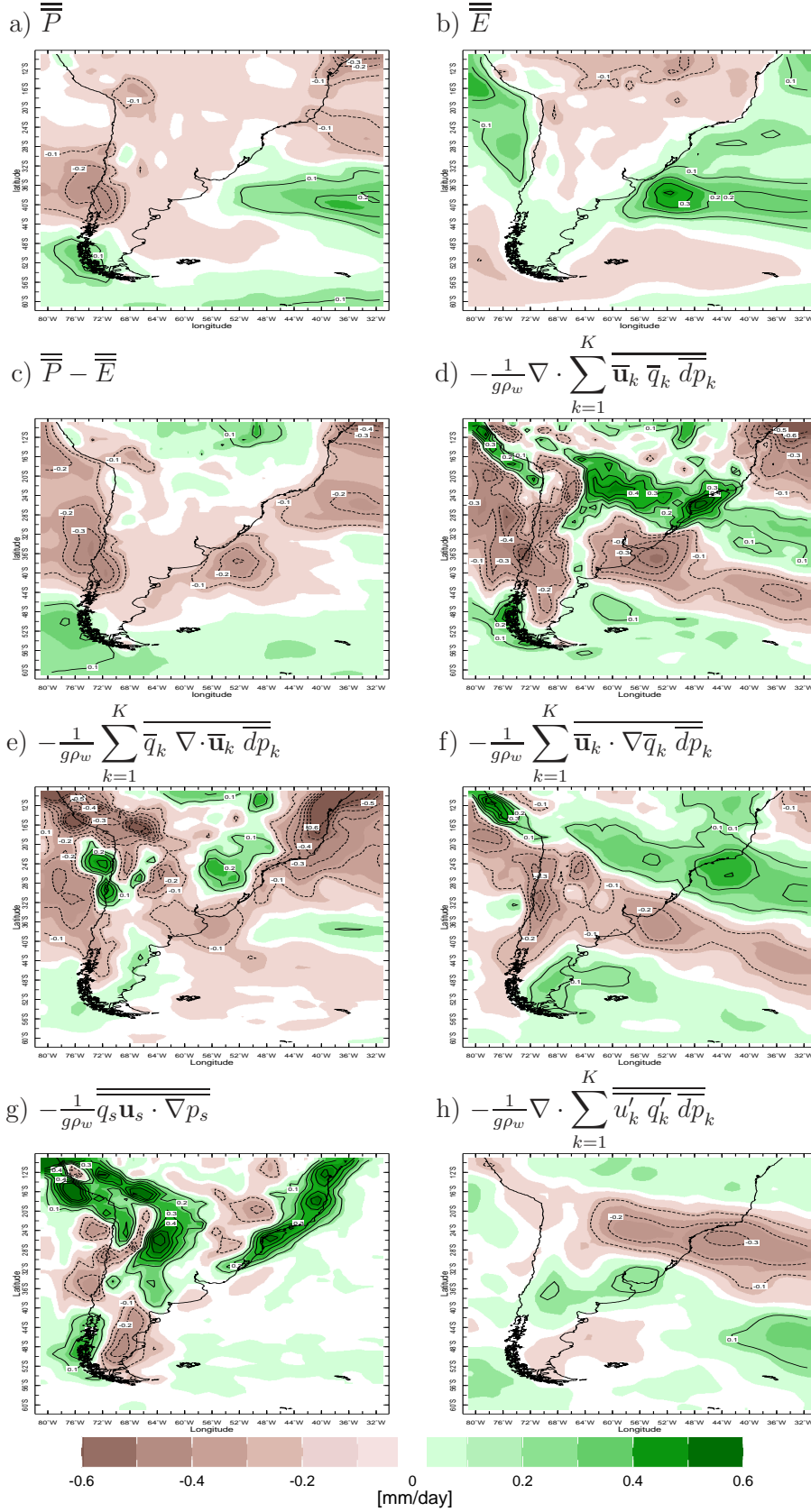


FIG. 12. Same as Figure 10 but for the South America region.

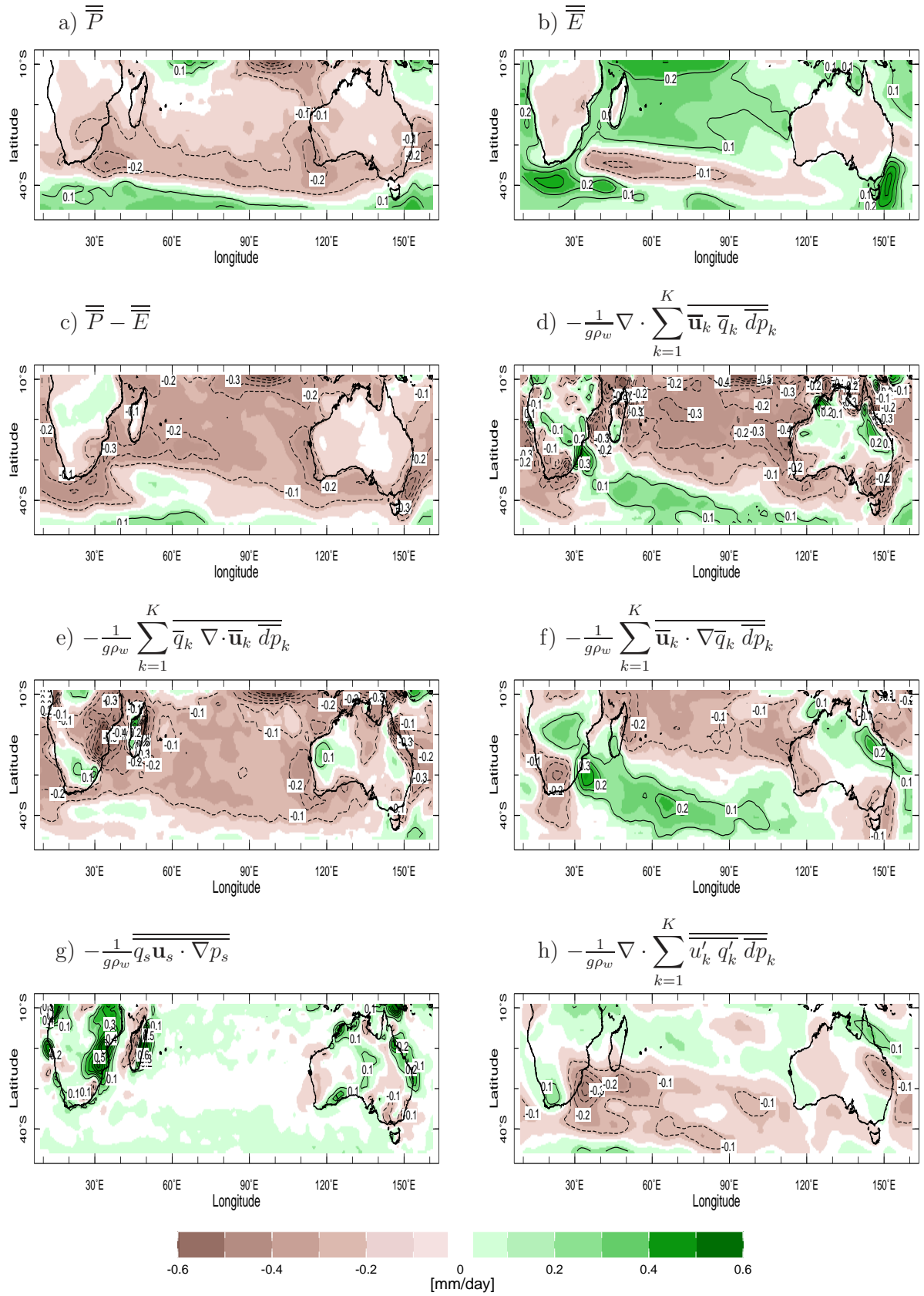


FIG. 13. Same as Figure 10 but for the Africa and Australia region.

CMIP5, South America, (2021-2040) - (1979-2005), JJAS

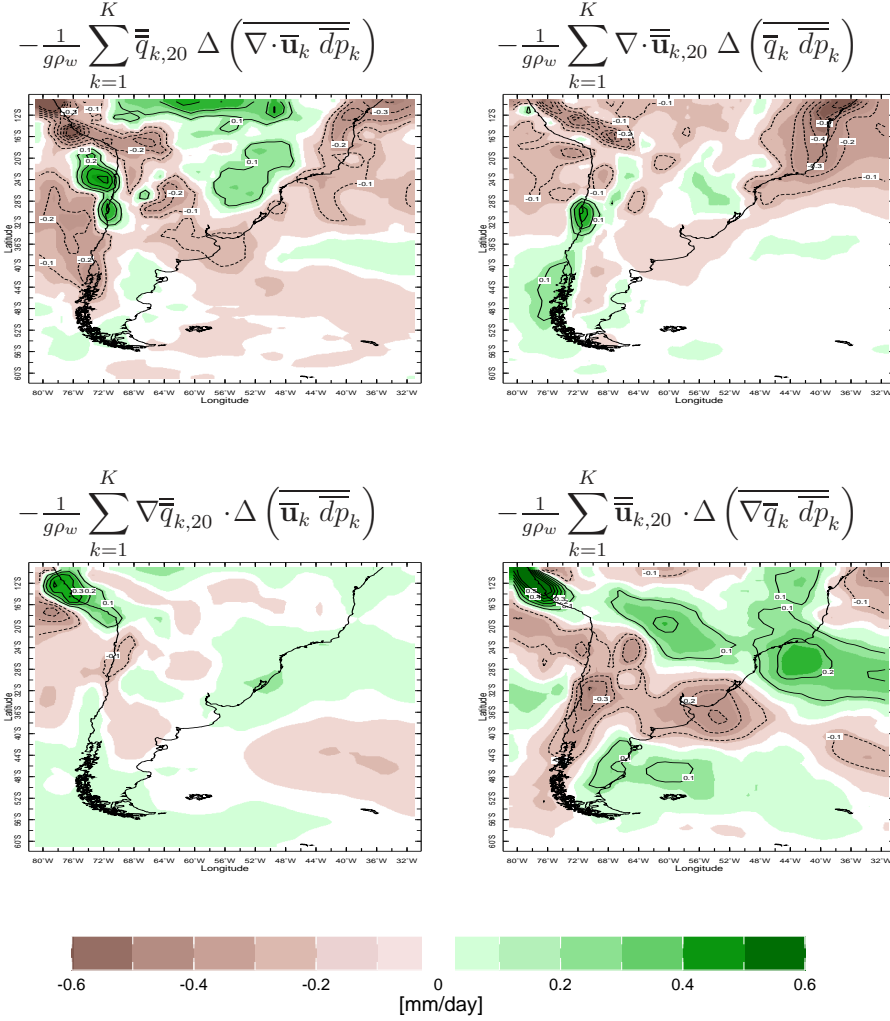


FIG. 14. Further breakdown of the CMIP5 multimodel mean-projected changes in the winter moisture budget here for the South America region. Changes in the mean flow moisture convergence are broken down into components due to circulation changes (dynamic component, left) and moisture changes (thermodynamic component, right) and related to mass divergence (upper) and moisture advection (lower). Units are mm/day.



CMIP5, Africa and Australia, (2021-2040) - (1979-2005), JJAS

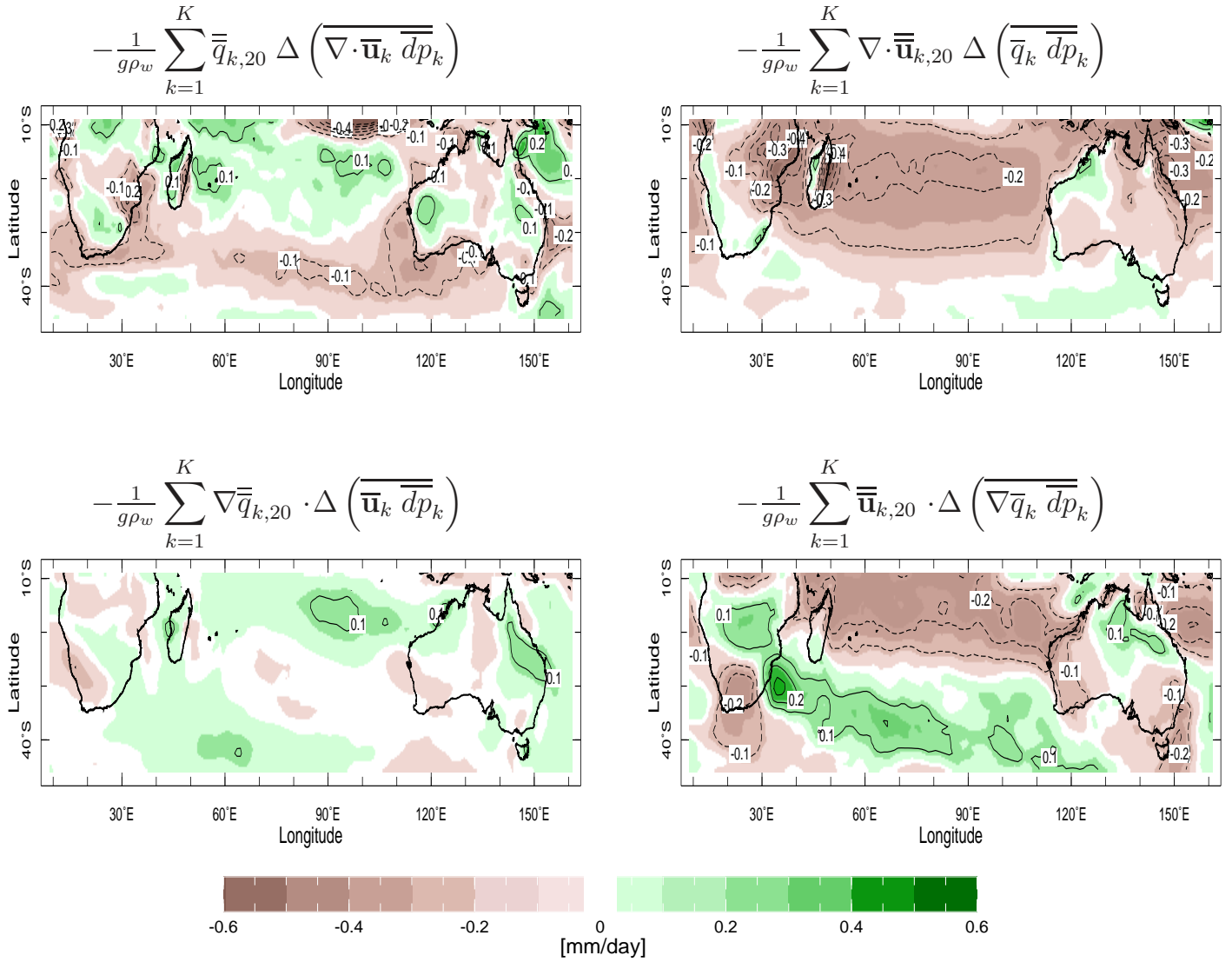
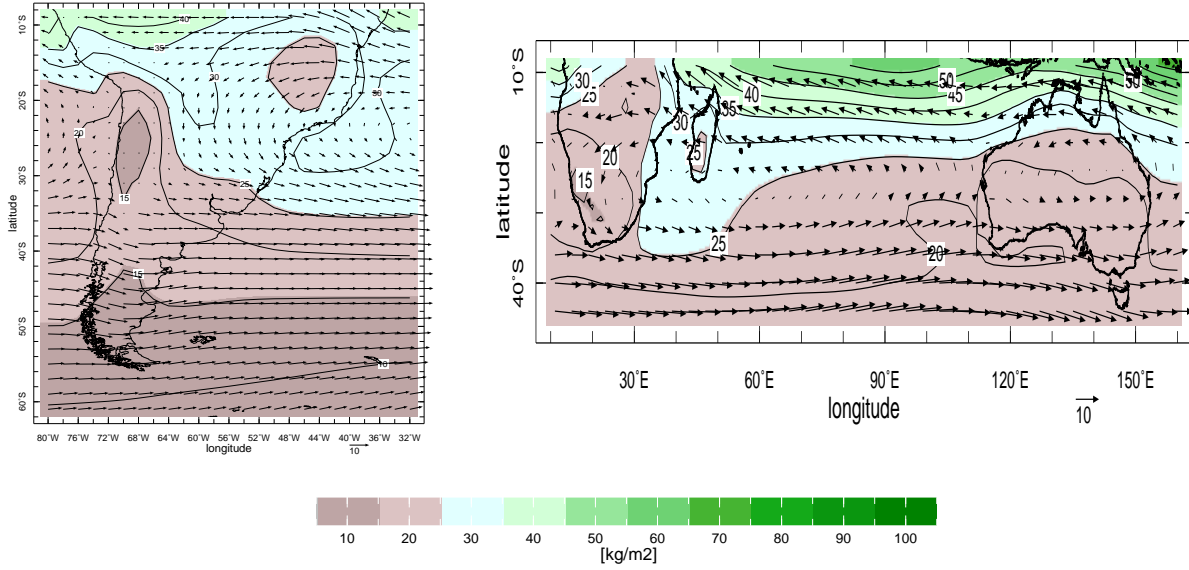


FIG. 15. Same as Figure 14 but for the Africa and Australia region.

$$\text{CMIP5, (1979-2005) JJAS Climatology (color), } \frac{1}{g} \sum_{k=1}^K \Delta \bar{q}_k \bar{d}p_k$$

(1979-2005) JJAS Climatology of 850hPa winds (vector, m/s)



$$\text{CMIP5, (2021-2040) - (1979-2005) JJAS (color), } \frac{1}{g} \sum_{k=1}^K \Delta \bar{q}_k \bar{d}p_k$$

(2021-2040) - (1979-2005) JJAS of 850hPa winds (vector, m/s)

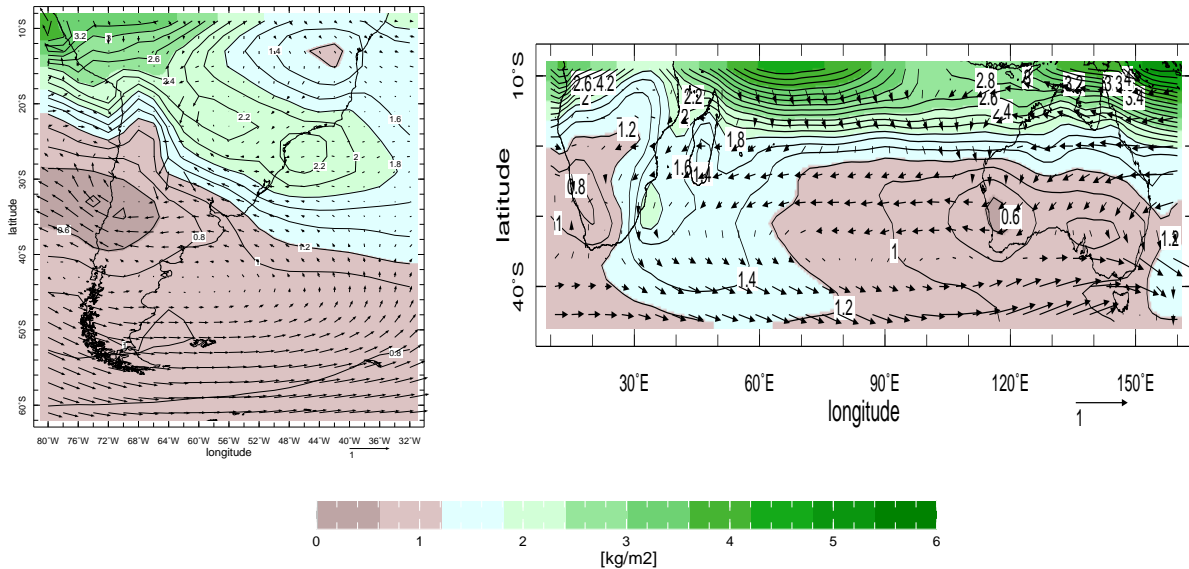
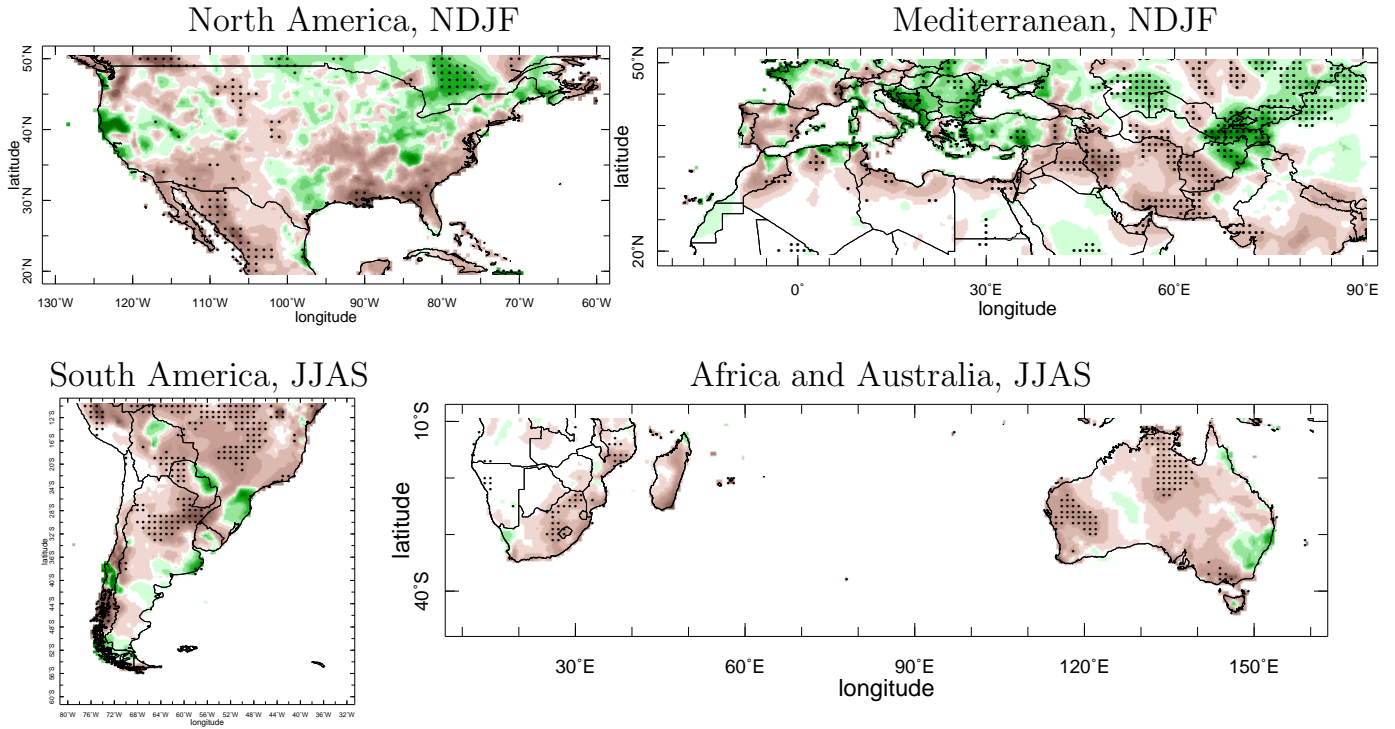


FIG. 16. The climatological specific humidity integrated from surface to 600hPa (color) and 850hPa winds (vectors) (top) and the 2021-2040 minus 1979-2005 change in these (bottom) for the southern hemisphere. Units are  $kg/m^2$  and  $m/s$ .

CRU TS3.25, Precipitation, (1997-2016) - (1971-1990), Significant (dots)



CMIP5, multi model mean  $\bar{P}$ , (1997-2016) - (1971-1990), Agreement (dots)

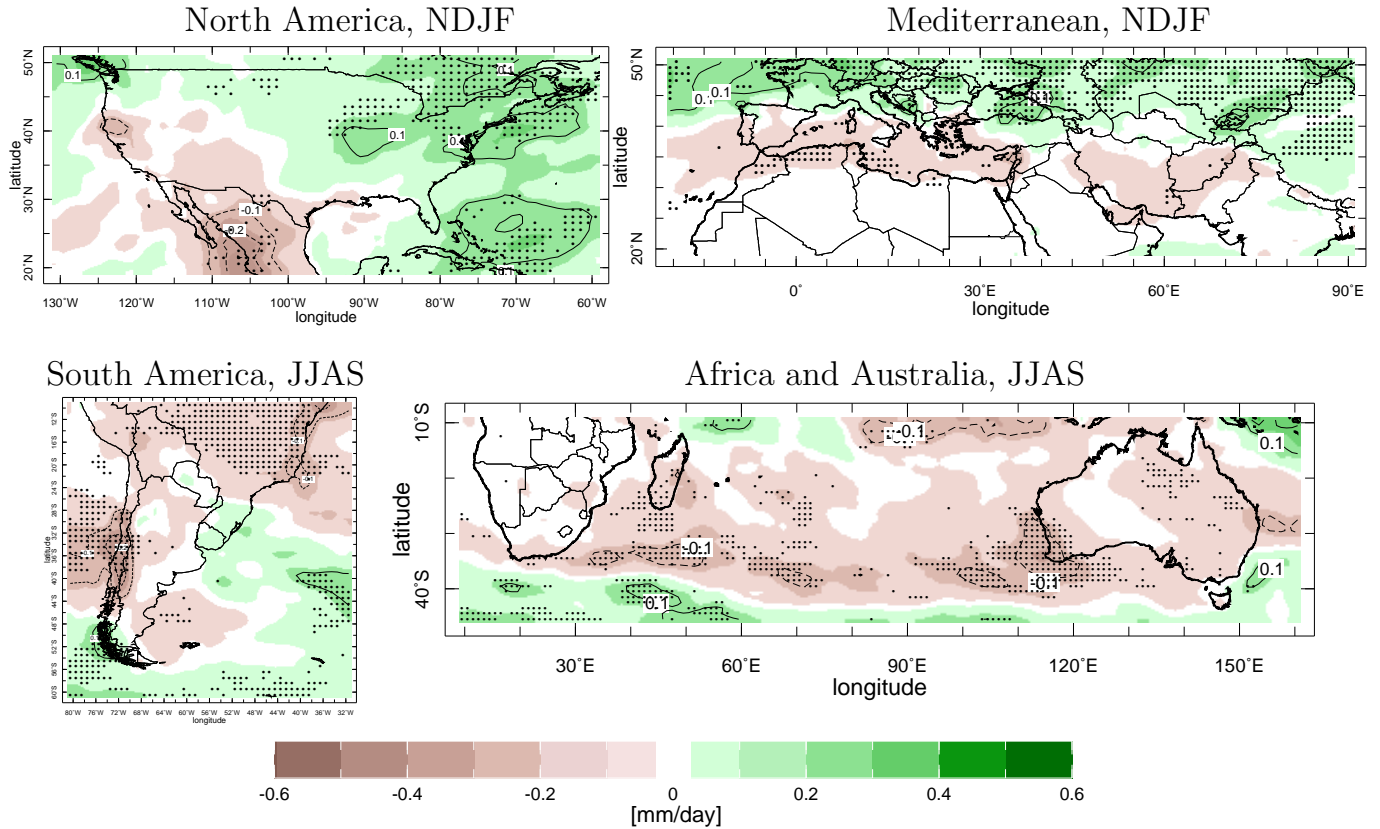


FIG. 17. Figure A1. The CRU TS3.25 observed (top) and CMIP5 multimodel mean (bottom) difference in winter precipitation for 1997-2016 minus 1971-1990. In the upper panel for the observed data the tick marks show where the differences between the means of the two-decade periods is significant at the 10% level according to a two-sided t-test. In the lower panel for the models the tick marks show where 3/4 of the models agree on the sign of the change and agree with the sign of the multimodel mean change. Units are  $mm/day$ .